The Astrophysical Journal, 660:1118–1136, 2007 May 1

COSMOLOGICAL EFFECTS OF POWERFUL AGN OUTBURSTS IN GALAXY CLUSTERS: INSIGHTS FROM AN *XMM-NEWTON* OBSERVATION OF MS 0735+7421

M. Gitti,[1,2] B. R. McNamara,[1,3,4] P. E. J. Nulsen,[4] and M. W. Wise[5]
Received 2006 September 21; accepted 2007 January 12

ABSTRACT

We report on the results of an analysis of *XMM-Newton* observations of MS 0735+7421, the galaxy cluster that hosts the most energetic AGN outburst currently known. The previous *Chandra* image shows twin giant X-ray cavities (∼200 kpc diameter) filled with radio emission and surrounded by a weak shock front. *XMM* data are consistent with these findings. The total energy in cavities and shock ($\sim 6 \times 10^{61}$ ergs) is enough to quench the cooling flow and, since most of the energy is deposited outside the cooling region (∼100 kpc), to heat the gas within 1 Mpc by $\sim\frac{1}{4}$ keV per particle. The cluster exhibits an upward departure (factor ∼2) from the mean *L-T* relation. The boost in emissivity produced by the ICM compression in the bright shells due to the cavity expansion may contribute to explain the high luminosity and high central gas mass fraction that we measure. The scaled temperature and metallicity profiles are in general agreement with those observed in relaxed clusters. Also, the quantities we measure are consistent with the observed *M-T* relation. We conclude that violent outbursts such as the one in MS 0735+7421 do not cause dramatic instantaneous departures from cluster scaling relations (other than the *L-T* relation). However, if they are relatively common they may play a role in creating the global cluster properties.

Subject headings: cooling flows — cosmology: miscellaneous — galaxies: clusters: general — galaxies: clusters: individual (MS 0735.7+7421) — intergalactic medium — X-rays: galaxies: clusters

1. INTRODUCTION

The current generation of X-ray satellites, *Chandra* and *XMM-Newton*, has shown that the physics of the intracluster medium (ICM) is complex and needs to be regulated by additional, nongravitational processes beyond the simple gravity and gas dynamics considered in the standard cold dark matter cosmological scenario (White & Rees 1978). In particular, our understanding of cooling flow systems has radically changed. Although it confirms the existence of short cooling times, high densities, and low temperatures in the cluster cores, the arrival of new high-resolution X-ray data has shown the lack of the emission lines expected from gas cooling below 1–2 keV and has reduced by about 1 order of magnitude the new spectroscopically derived mass deposition rates (e.g., David et al. 2001; Johnstone et al. 2002; Peterson et al. 2003, and references therein). The most plausible solution to this so-called "cooling flow problem" is that some form of additional heating that balances the cooling must be acting in the ICM. Among the many proposed heating mechanisms,[6] one of the best candidates for supplying the energy is feedback from the active galactic nucleus (AGN) hosted by the central galaxy of the cluster (e.g., Rosner & Tucker 1989; Tabor & Binney 1993; Churazov et al. 2001; Brüggen & Kaiser 2001; Kaiser & Binney 2003; Ruszkowski & Begelman 2002; Brighenti & Mathews 2003; Omma et al. 2004).

The possibility of AGN heating has recently become the leading idea to solve the cooling flow problem thanks to the discovery of X-ray cavities in the ICM on scales often approximately coincident with the lobes of extended radio emission (e.g., Hydra A: McNamara et al. 2000, David et al. 2001; Perseus: Böhringer et al. 1993, Churazov et al. 2000, Fabian et al. 2000; A2052: Blanton et al. 2001, 2003; A2597: McNamara et al. 2001, Pollack et al. 2005, Clarke et al. 2005; RBS797: Schindler et al. 2001, Gitti et al. 2006; A4059: Heinz et al. 2002). This finding indicates that the radio lobes fed by AGNs have displaced the X-ray-emitting gas, creating cavities in the ICM. These outbursts can be recurrent, as has been observed in some cases. For example, RBS797 shows evidence of a restarted AGN activity with precessing jets pointing to a different direction with respect to the one of the outer radio lobes filling the cavities (Gitti et al. 2006). The heating by AGNs is thought to occur through the dissipation of the cavity enthalpy and through shocks driven by the bubbles inflated by the AGN. Systematic studies of a sample of X-ray cavities show that their enthalpies[7] lie between 10^{55} and 10^{61} ergs and scale in proportion to the cooling X-ray luminosity and the radio power of the host system. In more than a half of the sample the energy input from the central radio source is currently sufficient to balance cooling (Bîrzan et al. 2004; Rafferty et al. 2006). The trend between X-ray luminosity and bubble mechanical luminosity, together with the existence of short central cooling time, suggests that the AGN is fueled by a cooling flow that is itself regulated by feedback from the AGN. The basic idea of

[1] Department of Physics and Astronomy, Ohio University, Athens, OH 45701.
[2] INAF–Osservatorio Astronomico di Bologna, 40127 Bologna, Italy.
[3] Department of Physics and Astronomy, University of Waterloo, Waterloo, ON N2L 2G1, Canada.
[4] Harvard-Smithsonian Center for Astrophysics, Cambridge, MA 02138.
[5] Astronomical Institute, University of Amsterdam, 1098 SJ Amsterdam, Netherlands.

[6] Proposed heating mechanisms include electron thermal conduction from the outer regions of clusters (Tucker & Rosner 1983; Voigt et al. 2002; Fabian et al. 2002; Zakamska & Narayan 2003), continuous subcluster merging (Markevitch et al. 2001), contribution of the gravitational potential of the cluster core (Fabian 2003), feedback from intracluster supernovae (Domainko et al. 2004), etc.

[7] The enthalpy (free energy) of the cavities is estimated from the total AGN power as $H = (\gamma/\gamma - 1)PV$, where the PV work done by the jet as it inflates the cavity is determined by measuring the cavity size and its surrounding pressure, and the adiabatic index γ is related to the internal composition of the cavities, still unknown. In the case of a relativistic plasma $\gamma = 4/3$ and $H = 4PV$.

this AGN-cooling-flow scenario is that a self-regulated equilibrium may be achieved, in which the energy input from the AGN balances the radiative losses of the ICM over the lifetime of the cluster.

The recent discovery of giant cavities and associated large-scale shocks in three systems (MS 0735+7241: McNamara et al. 2005; Hercules A: Nulsen et al. 2005a; Hydra A: Nulsen et al. 2005b) has shown that AGN outbursts not only can affect the central regions but can also have an impact on cluster-wide scales. In particular, the supercavities discovered in MS 0735+7421 have a diameter of about 200 kpc each, and a weak cocoon shock surrounding them has been detected. This large-scale outburst is the most powerful known so far: it releases upward of 10^{61} ergs into the ICM, heating the gas beyond the cooling region (McNamara et al. 2005). In this paper we want to investigate the significant consequences that this new development has for several fundamental problems in astrophysics. One important problem addressed by giant cavities is so-called cluster preheating, which is manifested in the steepening of the observed luminosity versus temperature relation for clusters with respect to theoretical predictions that include gravity alone (e.g., Markevitch 1998). Some extra nongravitational energy is required to explain such a steepening (e.g., Wu et al. 2000; Voit 2005), and one possibility is that it is supplied by a AGN outbursts. The additional nongravitational heating supplied by AGNs could also induce the suppression of the gas cooling in massive galaxies required to explain the exponential turnover at the bright end of the luminosity function of galaxies (Benson et al. 2003). This would indicate a common solution for the two major heating problems associated with the ICM: those of cooling flow and galaxy formation. Some cavities live longer than the time it takes to cross their own diameters, suggesting they are in pressure balance with the surrounding medium. Since the work required to inflate the radio lobes generally exceeds the nonthermal minimum energy of the radio emission (e.g., De Young 2006 and references therein), on the hypothesis that the assumptions adopted into the equipartition calculation are correct, some additional component besides the relativistic plasma may fill the cavity and contribute to support them internally. We want to investigate what is currently providing the necessary pressure support to sustain the cavities. Finally, in a more general view, we want to investigate what is the potential impact that such powerful outbursts have on the global properties of the ICM. Understanding well the ICM physics is essential to use galaxy clusters as high-precision cosmological tools.

We address these problems by studying the X-ray properties of the most energetic outburst known in a galaxy cluster. MS 0735+7421 (hereafter MS 0735) is at a redshift of 0.216. With a Hubble constant of $H_0 = 70\ \mathrm{km\ s^{-1}\ Mpc^{-1}}$ and $\Omega_M = 1 - \Omega_\Lambda = 0.3$, the luminosity distance is 1069 Mpc and the angular scale is 3.5 kpc $\mathrm{arcsec^{-1}}$.

2. OBSERVATION AND DATA PREPARATION

MS 0735 was observed by *XMM–Newton* in 2005 April during revolution 0973. In this paper only data from the European Photon Imaging Camera (EPIC) are analyzed and discussed, while those from the Reflection Grating Spectrometer (RGS) will be presented in a subsequent paper. The MOS and pn detectors were both operated in Full Frame Mode with the THIN filter, for an exposure time of 70.6 ks for MOS and 60.7 ks for pn. We use the SAS version 6.5.0 processing tasks `emchain` and `epchain` to generate calibrated event files from raw data. Throughout this analysis single pixel events for the pn data (PATTERN 0) are selected, while for the MOS data sets the PATTERNs 0–12 are used. The removal of bright pixels and hot columns is done in a conservative way applying the expression (FLAG==0). To reject the soft proton flares we accumulate the light curve in the [10–12] keV band for MOS and [12–14] keV band for pn, where the emission is dominated by the particle–induced background, and exclude all the intervals of exposure time having a count rate higher than a certain threshold value (the chosen threshold values are 0.4 counts $\mathrm{s^{-1}}$ for MOS and 0.7 counts $\mathrm{s^{-1}}$ for pn). The remaining exposure times after cleaning are 50.4 ks for MOS1, 49.5 ks for MOS2, and 42.0 ks for pn. Starting from the output of the SAS detection source task, we make a visual selection on a wide energy band MOS and pn image of point sources in the field of view. Events from these regions are excluded directly from each event list. The source and background events are corrected for vignetting using the weighted method described in Arnaud et al. (2001), the weight coefficients being tabulated in the event list with the SAS task `evigweight`. This allows us to use the on-axis response matrices and effective areas. Unless otherwise stated, the reported errors are at 90% confidence level.

2.1. *Background Treatment*

The background estimates are obtained using a blank-sky observation consisting of several high-latitude pointings with sources removed (Lumb et al. 2002). The blank-sky background events are selected using the same selection criteria (such as PATTERN, FLAG, etc.), intensity filter (for flare rejection), and point-source removal used for the observation events. This yields final exposure times for the blank fields of 365 ks for MOS1, 350 ks for MOS2, and 294 ks for pn. Since the cosmic-ray-induced background might change slightly with time, we compute the ratio of the total count rates in the high-energy band ([10–12] keV for MOS and [12–14] keV for pn). The obtained normalization factors (1.266, 1.303, 1.283 for MOS1, MOS2, and pn, respectively) are then used to renormalize the blank field data. The blank-sky background files are recast in order to have the same sky coordinates as MS 0735.

The usual approach to performing the background subtraction is described in full detail in Arnaud et al. (2002). This procedure consists of two steps. In a first step, for each product extracted from the observation event list an equivalent product is extracted from the corresponding blank-field file and then subtracted from it. This allows us to remove the particle background. However, if the background in the observation region is different from the average background in blank field data, this step could leave a residual background component. The residual background component is estimated by using blank-field-subtracted data in a region free of cluster emission (in particular we consider an annulus lying between $8'$ and $10'$), which are then subtracted in a second step from each MOS and pn product. In our case the residual is negative in the energy band adopted for the spatial analysis ([0.4–2] keV; see § 3.1). The residual count rate summed over the three detectors is -0.07 counts $\mathrm{s^{-1}}$, which represents $\sim$10% of the total background count rate in this energy band.

The fluorescent emission lines[8] excited by the energetic charged particles that pass through the detector exhibit spatial variation over the detector. This effect would compromise the reliability of the second step of the background subtraction for spectra, as the resulting total background spectrum (sum of the particle background spectrum, estimated in the blank-field-subtracted cluster region, and the residual background component, estimated in the blank-field-subtracted outer annular region) shows fluorescence lines that are shifted by a few energy channels with respect to the

[8] Al and Si lines at 1.5 and 1.7 keV, respectively, in the MOS data, and Ni, Cu, and Zn lines around 8 keV in the pn data.

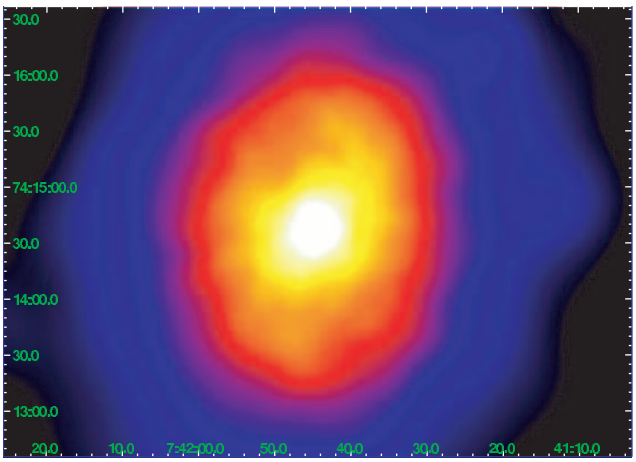

FIG. 1.—MOS1 image of MS 0735 in the [0.3–10] keV energy band. The image is corrected for vignetting and exposure and is adaptively smoothed (S/N = 20).

MS 0735 spectrum. Therefore, the residual background component is neglected for the purpose of the spectral analysis.

3. MORPHOLOGICAL ANALYSIS

The adaptively smoothed, exposure corrected MOS1 count rate image in the [0.3–10] keV energy band is presented in Figure 1. The smoothed image is obtained from the raw image corrected for the exposure map (that accounts for spatial quantum efficiency, mirror vignetting, and field of view) by running the task `asmooth` set to a desired signal-to-noise ratio (S/N) of 20. Regions exposed with less than 10% of the total exposure are not considered.

The inner part of the cluster shows the high surface brightness characteristic of a cooling flow. We notice a sharp central surface brightness peak at a position $\alpha = 07^{h}41^{m}44.06^{s}$, $\delta = +74^{\circ}14'38.62''$ (J2000.0). At small radii, two strong depressions with a diameter of about 150 kpc (see § 3.1) are visible on opposite side of the cluster center in the northeast-southwest direction. The cavities are surrounded by a bright X-ray emission of elliptical shape, in the form expected by a radio cocoon. The elliptical discontinuity in the X-ray surface brightness appears more evident in the *Chandra* data and has been interpreted as a weak shock (McNamara et al. 2005). Beyond the cavity region the cluster maintains a slightly elliptical morphology up to large radii, showing hints of structures that could be the results of past radio activity that created older cavities.

3.1. *Surface Brightness Profile*

We consider different sectors to the north and south (N sector: between 10° west and 60° east of north; S sector: between 15° east and 60° west of south) and to the east and west (E sector: between 30° north and 75° south of east; W sector: between 30° south and 80° north of west) in order to include and exclude the cavity regions, respectively. We also consider a full 360° sector in which we mask the cavities (hereafter undisturbed cluster). For each sector, we compute a background-subtracted, vignetting-corrected, radial surface brightness profile in the [0.4–2] keV energy band for each camera separately. For the pn data, we generate a list of out-of-time events (OoTs)[9] to be treated as an additional background component. The effect of OoTs in the current observing mode (full frame) is 6.3%. The OoT list is processed in a similar way as is done for the pn observation event file. The profiles for the three detectors are then added into a single profile, binned such that a S/N of at least 3 is reached.

[9] Out-of-time events are caused by photons which arrive while the CCD is being read out, and are visible in an uncorrected image as a bright streak smeared out in RAWY.

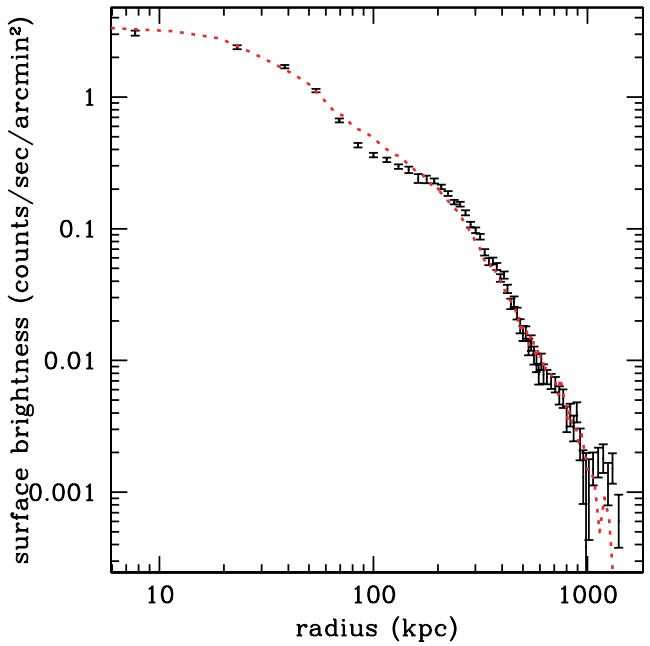

FIG. 2.—Background subtracted, azimuthally averaged radial surface brightness profile of the N sector data in the [0.4–2] keV range. The dotted red line shows the profile in full 360° sector with masked cavities (undisturbed cluster). A deficit of emission in the N sector between radii of ~50–200 kpc is visible.

The cluster emission is detected up to 1.3 Mpc (~6′). In Figure 2 we show the X-ray surface brightness profile for the sector containing the northern cavity compared with that of the undisturbed cluster. We note that the data of the undisturbed cluster appear regular, while those for the N sector show a clear deficit of emission between radii ~50 and ~200 kpc relative to the other directions. The S sector profile shows a behavior similar to the N sector, although the depression is less pronounced, whereas the E and W sectors appear regular.

The surface brightness profile of the undisturbed cluster is fitted in the CIAO tool `Sherpa` with various parametric models, which are convolved with the *XMM* point-spread function (PSF). The overall PSF is obtained by adding the PSF of each camera (Ghizzardi 2001), estimated at an energy of 1.5 keV and weighted by the respective cluster count rate in the [0.4–2] keV energy band. A single β-model (Cavaliere & Fusco-Femiano 1976) is not a good description of the entire profile: a fit to the outer regions shows a strong excess in the center as compared to the model (see Fig. 3). The centrally peaked emission is a strong indication of a cooling flow in this cluster. We find that for 100 kpc $\lesssim r \lesssim$ 1150 kpc the data can be described ($\chi^2_{\rm red} \sim 1.65$ for 87 dof) by a β-model with a core radius $r_c = 195 \pm 4$ kpc and a slope parameter $\beta = 0.77 \pm 0.01$ (3 σ confidence level). The single β-model functional form is a convenient representation of the gas density profile in the outer regions, which is used as a tracer for the potential. This best-fit model is thus used in the following to estimate the cluster gas and total mass profiles (see § 6).

We also consider a double isothermal β-model and find that it can account for the entire profile when the very inner and outer regions are excluded: for 10 kpc $\lesssim r \lesssim$ 1150 kpc the best-fit parameters are $r_{c1} = 200 \pm 4$ kpc, $\beta_1 = 0.77 \pm 0.01$, $r_{c2} = 116 \pm 8$ kpc, $\beta_2 = 4.67 \pm 0.56$; $\chi^2_{\rm red} \sim 1.87$ for 96 dof. By assuming a

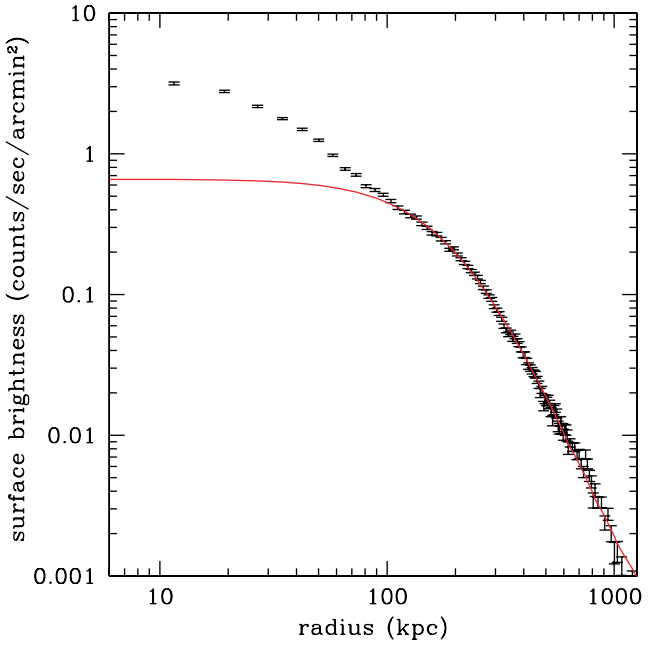

FIG. 3.—Background subtracted, azimuthally averaged radial surface brightness profile in the [0.4–2] keV range. The best-fit β-model fitted over the 100–1150 kpc region is overplotted as a solid red line. In the central region, the observed surface brightness profile shows a strong excess as compared to the extrapolation of the model.

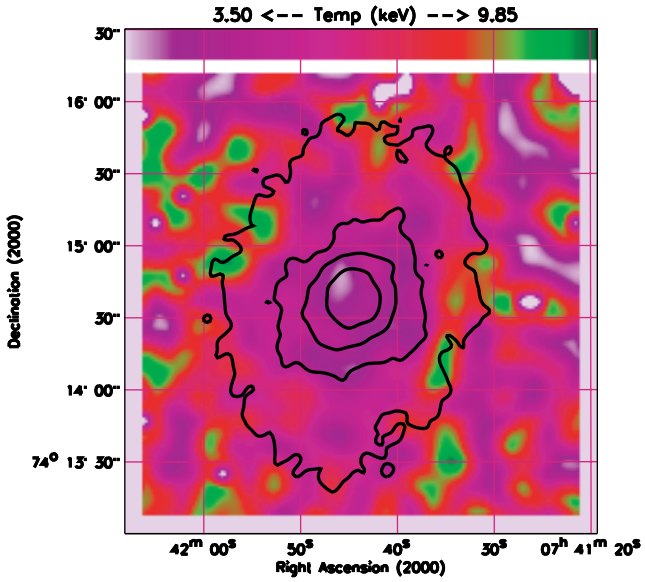

FIG. 4.—Temperature map obtained by using four X-ray colors ([0.3–1.0], [1.0–2.0], [2.0–4.5], [4.5–8.0] keV) and estimating the expected count rate with XSPEC for a thermal `mekal` model, with fixed absorbing column $N_{\rm H} = 3.49 \times 10^{20}$ atom cm^{-2} and metallicity $Z = 0.4\ Z_{\odot}$. The metallicity gradient in the central region (see Fig. 6) does not affect the map significantly. The map has a pixel size of 1.1″ and is smoothed with a Gaussian of $\sigma = 16.5''$. Superposed are the X-ray contours. The features outside the last contours are not significant, as they are mainly due to noise fluctuations.

common β-value we find: $r_{c1} = 215 \pm 4$ kpc, $r_{c2} = 30 \pm 2$ kpc, $\beta = 0.79 \pm 0.01$; $\chi^2_{\rm red} \sim 2.08$ for 97 dof.

4. TEMPERATURE MAP

The temperature image of the cluster central region shown in Figure 4 is built from X-ray colors. Specifically, we extract mosaicked MOS images in four different energy bands ([0.3–1.0], [1.0–2.0], [2.0–4.5], and [4.5–8.0] keV), subtract the background and divide the resulting images by the exposure maps. A temperature in each pixel of the map is obtained by fitting values in each pixel of these images with a thermal plasma, fixing $N_{\rm H}$ to the Galactic value (Dickey & Lockman 1990) and the element abundance to 0.4 solar (see § 5.1). Besides the evidence that the very central region is cooler than the surrounding medium, we do not notice any particular structure in the temperature distribution.

The regularity of the temperature distribution points to a relaxed dynamical state of the cluster, thus excluding the presence of an ongoing merger. Since cluster merging can cause strong deviations from the assumption of an equilibrium configuration, this allows us to derive a good estimate of the cluster mass (see § 6).

5. SPECTRAL ANALYSIS

Throughout the analysis, a single spectrum is extracted for each region of interest and is then regrouped to give at least 25 counts in each bin. The data are modeled using the XSPEC code, version 11.3.0. Unless otherwise stated, the relative normalizations of the MOS and pn spectra are left free when fitted simultaneously. We use the following response matrices:

`m1_534_im_pall_v1.2.rmf` (MOS1),
`m2_534_im_pall_v1.2.rmf` (MOS2),
`epn_ff20_sY9_v6.7.rmf` (pn).

5.1. *Global Spectrum*

For each instrument, a global spectrum is extracted from all events lying within 6′ of the cluster emission peak, which corresponds to the outermost radius determined from the morphological analysis (§ 3.1). We test in detail the consistency between the three cameras by fitting separately these spectra with an absorbed `mekal` model with the redshift fixed at $z = 0.216$ and the absorbing column fixed at the Galactic value ($N_{\rm H} = 3.49 \times 10^{20}$ atoms cm^{-2}; Dickey & Lockman 1990) and studying the effect of imposing various high and low-energy cutoffs. We find good agreement between the three cameras in the [0.4–10.0] keV energy range ($kT = 4.62^{+0.19}_{-0.18}$ keV for MOS1, 4.34 ± 16 keV for MOS2, $4.37^{+0.13}_{-0.11}$ keV for pn).

The combined MOS+pn global temperature (in keV) and metallicity (as a fraction of the solar value, Anders & Grevesse 1989) derived from the best fit ($\chi^2_{\rm red} \sim 1.18$ for 1947 dof) are, respectively, $kT = 4.43^{+0.09}_{-0.08}$ keV and $Z = 0.35^{+0.03}_{-0.03}\ Z_{\odot}$. The unabsorbed luminosities in this model (estimated from the average of the fluxes measured by the three cameras after fixing $N_{\rm H} = 0$) in the X-ray ([2.0–10.0] keV) and bolometric band are, respectively, $L_{\rm X} = 4.61 \pm 0.04 \times 10^{44}$ and $L_{\rm bol} = 1.05 \pm 0.01 \times 10^{45}$ ergs s^{-1}, where the errors are given as half the difference between the maximum and the minimum value.

5.2. *Projected Radial Profiles: Temperature and Metallicity*

We produce projected radial temperature and metallicity profiles by extracting spectra in circular annuli centered on the peak of the X–ray emission. The annular regions are detailed in Table 1. The data from the three cameras are modeled simultaneously using a simple, single-temperature model (`mekal` plasma emission code in XSPEC) with the absorbing column density fixed at the nominal Galactic value. The free parameters in this model are the temperature kT, metallicity Z (measured relative to the solar values, with the various elements assumed to be present in

TABLE 1
Spectral Fitting in Concentric Annular Regions

Radius (kpc)	kT (keV)	Z ($Z_\odot$)	χ^2/dof
0–70 (0″–20″)	$3.68^{+0.10}_{-0.10}$	$0.62^{+0.07}_{-0.07}$	694/641
70–140 (20″–40″)	$4.53^{+0.16}_{-0.15}$	$0.41^{+0.06}_{-0.07}$	695/652
140–210 (40″–1.0′)	$5.48^{+0.24}_{-0.23}$	$0.32^{+0.07}_{-0.07}$	715/617
210–315 (1′–1.5′)	$5.65^{+0.25}_{-0.23}$	$0.27^{+0.06}_{-0.06}$	718/690
315–420 (1.5′–2′)	$5.17^{+0.33}_{-0.31}$	$0.24^{+0.09}_{-0.09}$	484/505
420–630 (2′–3′)	$5.32^{+0.48}_{-0.42}$	$0.25^{+0.12}_{-0.12}$	582/599
630–945 (3′–4.5′)	$3.83^{+0.45}_{-0.37}$	$0.44^{+0.21}_{-0.18}$	858/739
945–1260 (4.5′–6′)	$2.80^{+1.33}_{-1.18}$	$1.11^{+3.37}_{-0.94}$	1129/810

Notes.—Results of the spectral fitting in concentric annular regions in the [0.4–10.0] keV energy range obtained by fixing the absorbing column density to the Galactic value ($N_{\rm H} = 3.49 \times 10^{20}$ cm^{-2}). The temperature (in keV) and metallicity (in fraction of the solar value; Anders & Grevesse 1989) are left as free parameters. Error bars are at the 90% confidence levels on a single parameter of interest.

their solar ratios, Anders & Grevesse 1989) and normalization (emission measure). The best-fitting parameter values and 90% confidence levels derived from the fits to the annular spectra are summarized in Table 1.

The projected temperature profile determined with this model is shown in Figure 5. It shows a rise from a mean value of $\sim$3.7 keV within 70 kpc to $\sim$5.4 keV over the 150–630 kpc region; then it declines to a value $\sim$2.8 keV in the outskirts of the cluster (up to 1.3 Mpc).

The metallicity profile is shown in Figure 6: a gradient is visible toward the central region, the metallicity increasing from $Z \sim 0.27\,Z_\odot$ over the 150–630 kpc region to $Z \sim 0.62\,Z_\odot$ inside the central 70 kpc. Due to the poor photon statistics, which prevents us from deriving accurate measurements, we exclude the last two bins.

We also perform the spectral fitting by leaving the absorbing column density as a free parameter, and find little variation in the results.

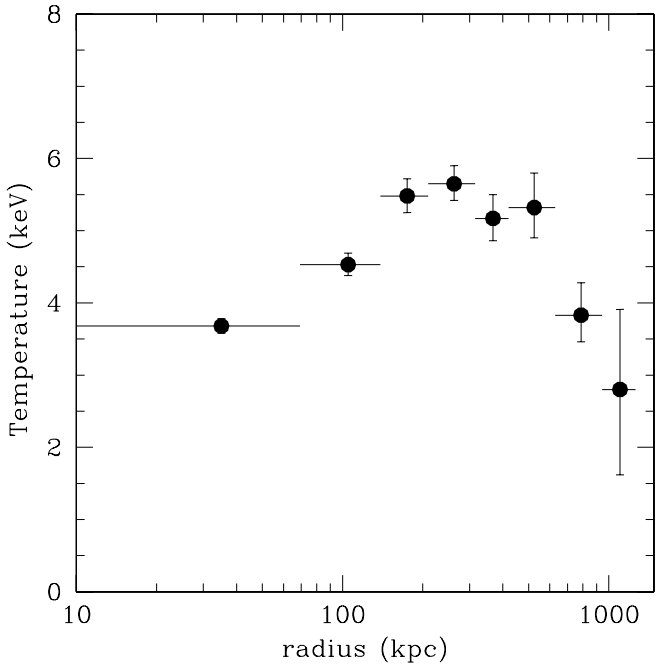

Fig. 5.—Projected X-ray gas temperature profile measured in the [0.4–10.0] keV energy range.

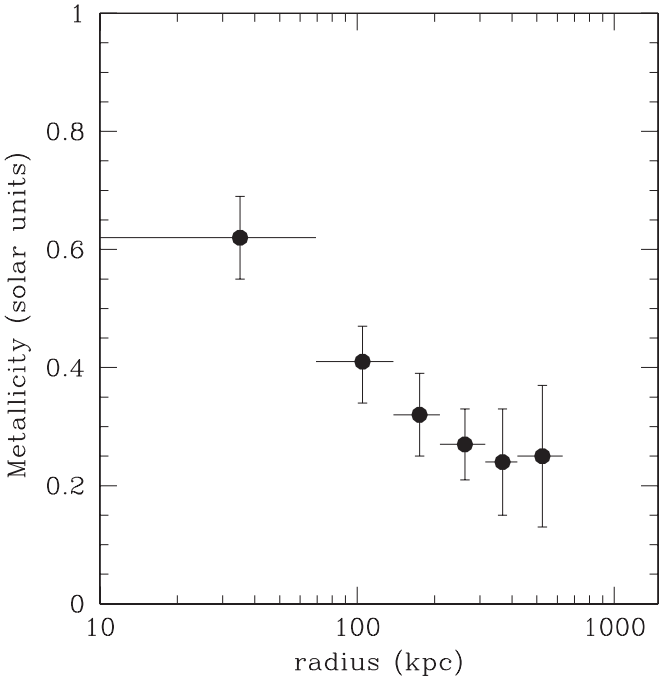

Fig. 6.—Projected X-ray gas metallicity profile measured in the [0.4–10.0] keV energy range. The last two bins have been excluded due to poor photon statistics.

5.3. *Deprojection Analysis: Temperature, Density, Pressure, and Entropy Profiles*

Because of projection effects, the spectral properties at any point in the cluster are the emission-weighted superposition of radiation originating at all points along the line of sight through the cluster. To correct for this effect of projection, we perform a deprojection analysis on the same annular spectra used in § 5.2 by adopting the XSPEC `projct` model. Under the assumption of ellipsoidal (in our specific case, spherical) shells of emission, this model calculates the geometric weighting factor according to which the emission is redistributed among the projected annuli.

The deprojection analysis is performed separately for the MOS1+MOS2 and pn spectra. The results are reported in Table 2, and the corresponding deprojected temperature and metallicity profiles are shown in Figures 7 and 8, respectively. We also perform the deprojection analysis by fitting simultaneously the spectra of the three cameras. In general, the results obtained from pn spectra appear more reliable, as the deprojected MOS and combined MOS+pn temperature profiles show some signs of instability, and we do not manage to derive a temperature estimate in the last annulus. In the following general discussion and in the estimate of the cluster mass derived from the density and temperature profiles (see § 6), we therefore adopt the pn deprojection results. As expected, the deprojected central temperature is lower than the projected one, since in the projected fits the spectrum of the central annulus is contaminated by hotter emission along the line of sight.

In Figures 9–11 we show various quantities derived from the deprojected spectral fits. The electron density n_e (Fig. 9) is obtained from the estimate of the emission integral $\mathrm{EI} = \int n_e n_p\, dV$ given by the `mekal` normalization: $10^{-14}\mathrm{EI}/\{4\pi[D_A(1+z)]^2\}$, where D_A is the angular size distance to the source. We assume $n_p = 0.82 n_e$ in the ionized intracluster plasma. By starting from the density and temperature information derived from the deprojection analysis, we can calculate the pressure profile (Fig. 10) as $P = nkT$, where we assume $n = 2n_e$. The average pressure

TABLE 2
DEPROJECTION ANALYSIS

	MOS1+MOS2				pn			
RADIUS (kpc)	kT (keV)	Z ($Z_\odot$)	Norm ($\times 10^{-4}$)	n_e (cm^{-3})	kT (keV)	Z ($Z_\odot$)	Norm ($\times 10^{-4}$)	n_e (cm^{-3})
0–70	$3.65^{+0.20}_{-0.19}$	$0.80^{+0.16}_{-0.15}$	$7.37^{+0.36}_{-0.36}$	$0.0210^{+0.0046}_{-0.0046}$	$3.20^{+0.18}_{-0.18}$	$0.59^{+0.15}_{-0.12}$	$8.45^{+0.42}_{-0.36}$	$0.0225^{+0.0050}_{-0.0046}$
70–140	$3.57^{+0.33}_{-0.28}$	$0.77^{+0.23}_{-0.20}$	$6.64^{+0.48}_{-0.49}$	$0.0075^{+0.0020}_{-0.0020}$	$4.19^{+0.43}_{-0.39}$	$0.33^{+0.16}_{-0.14}$	$9.55^{+0.41}_{-0.58}$	$0.0090^{+0.0019}_{-0.0022}$
140–210	$6.24^{+1.03}_{-0.78}$	$0.21^{+0.19}_{-0.19}$	$8.86^{+0.47}_{-0.45}$	$0.0053^{+0.0012}_{-0.0012}$	$4.86^{+0.79}_{-0.63}$	$0.47^{+0.23}_{-0.22}$	$7.55^{+0.55}_{-0.48}$	$0.0049^{+0.0013}_{-0.0012}$
210–315	$6.10^{+0.68}_{-0.51}$	$0.37^{+0.16}_{-0.15}$	$12.87^{+0.53}_{-0.55}$	$0.0035^{+0.0007}_{-0.0007}$	$5.80^{+0.83}_{-0.71}$	$0.22^{+0.16}_{-0.14}$	$11.63^{+0.53}_{-0.49}$	$0.0033^{+0.0007}_{-0.0007}$
315–420	$5.00^{+0.75}_{-0.57}$	$0.21^{+0.20}_{-0.17}$	$8.65^{+0.71}_{-0.53}$	$0.0020^{+0.0006}_{-0.0005}$	$4.90^{+0.89}_{-0.68}$	$0.25^{+0.18}_{-0.17}$	$8.66^{+0.53}_{-0.48}$	$0.0020^{+0.0005}_{-0.0005}$
420–630	$6.00^{+1.05}_{-0.85}$	$0.30^{+0.26}_{-0.23}$	$7.12^{+0.49}_{-0.48}$	$0.0009^{+0.0002}_{-0.0002}$	$6.37^{+1.84}_{-1.37}$	$0.12^{+0.29}_{-0.12}$	$6.23^{+0.37}_{-0.48}$	$0.0009^{+0.0002}_{-0.0002}$
630–945	$3.56^{+0.52}_{-0.43}$	$0.50^{+0.33}_{-0.26}$	$5.29^{+0.61}_{-0.59}$	$0.0004^{+0.0002}_{-0.0001}$	$4.83^{+1.70}_{-1.13}$	$0.15^{+0.37}_{-0.15}$	$5.34^{+0.54}_{-0.55}$	$0.0004^{+0.0001}_{-0.0001}$
945–1260	...	...	...	...	$2.71^{+1.70}_{-1.01}$	$1.59^{+5.99}_{-1.21}$	$0.98^{+0.64}_{-0.66}$	$0.0001^{+0.0001}_{-0.0001}$

NOTES.—Results of the deprojection analysis on annular MOS and pn spectra using the XSPEC `projct×tbabs×mekal` model. The column density is fixed to the Galactic value and the normalizations are in units of $10^{-14} n_e n_p V/4\pi[D_A(1+z)]^2$. The fits give χ^2/dof = 3160/2610 and 2786/2635 for MOS and pn, respectively.

surrounding the cavities is $\sim 6 \times 10^{-11}$ ergs cm^{-3}. Similarly, the entropy profile (Fig. 11) is calculated from the temperature and density profiles by using the commonly adopted definition $S = kTn_e^{-2/3}$. Allowing for the different resolutions of *Chandra* and *XMM*, the high central entropy level of about 40 keV cm^2 that we measure is in agreement with the value of about 30 keV cm^2 measured with *Chandra* (McNamara et al. 2005). As pointed out by Voit & Donahue (2005), this is consistent with being the result of the accumulation of the very energetic kinetic power outburst at the cluster center.

We investigate the effect of changing the radial binning by performing a similar spectral analysis (projected and deprojected) on different annular regions. We find results consistent with those presented in §§ 5.2 and 5.3. We also note that the results presented here are in agreement with those derived from the analysis of *Chandra* data (McNamara et al. 2005).

5.4. *Cooling Flow*

MS 0735 was identified as a candidate "cooling flow" cluster because of extended Hα emission from its central galaxy (Donahue et al. 1992) and *ROSAT* HRI detection of a central high surface brightness peak (Donahue & Stocke 1995). However, this identification still has to be confirmed by a detailed X-ray spectral analysis.

The surface brightness profile, temperature map, and temperature profile derived from our *XMM* data analysis give indications of the presence of a cooling core. Here we further investigate the physical properties of the ICM in the central region. The cooling time is calculated as the time taken for the gas to radiate its enthalpy per unit volume H using the instantaneous cooling rate at any temperature:

$$t_{\rm cool} \approx \frac{H}{n_e n_{\rm H} \Lambda(T)} = \frac{\gamma}{\gamma - 1} \frac{kT}{\mu X_{\rm H} n_e \Lambda(T)}, \quad (1)$$

where $\gamma = 5/3$ is the adiabatic index, $\mu \approx 0.61$ (for a fully ionized plasma) is the molecular weight, $X_{\rm H} \approx 0.71$ is the hydrogen

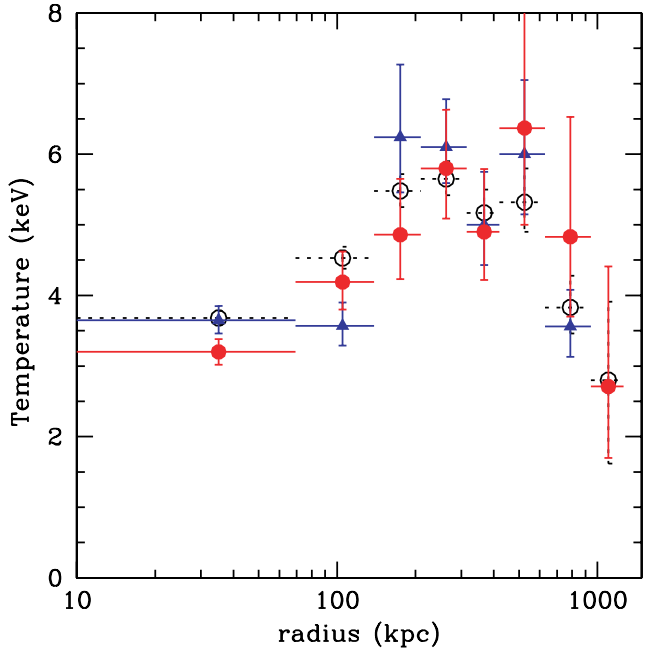

FIG. 7.—Deprojected X-ray gas temperature profile measured from MOS1+MOS2 (*blue triangles*) and pn (*red filled circles*) spectra. For comparison, the projected profile is also shown (*black open circles*).

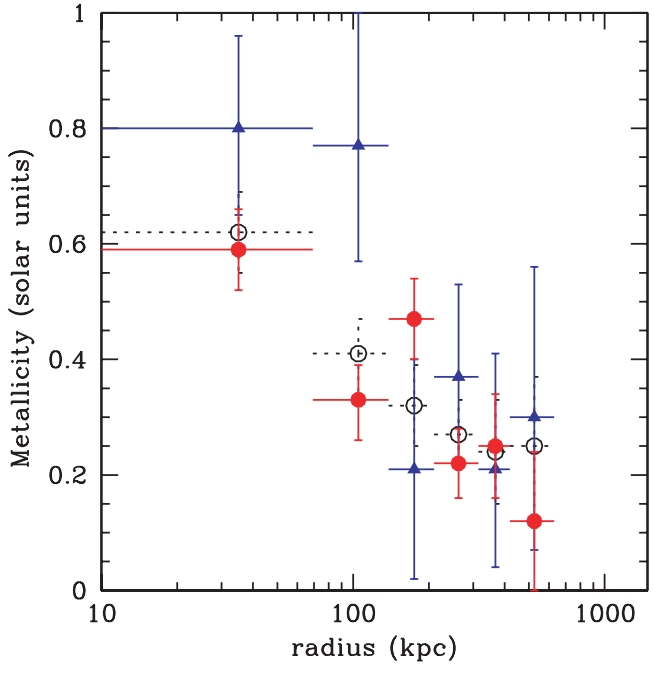

FIG. 8.—Deprojected X-ray gas metallicity profile measured from MOS1+MOS2 (*blue triangles*) and pn (*red filled circles*) spectra. For comparison, the projected profile is also shown (*black open circles*). The last two bins have been excluded due to poor photon statistics.

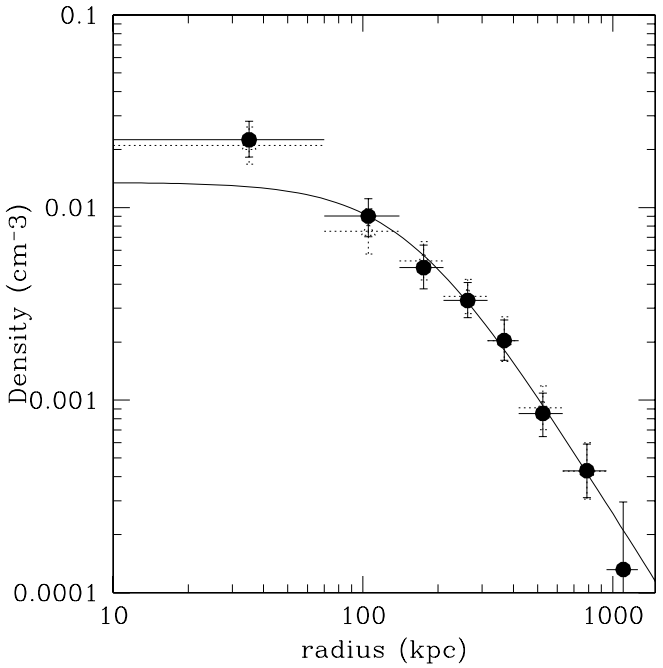

FIG. 9.—Electron density profile measured from pn spectra (*filled circles*). For comparison, the profile measured from MOS1+MOS2 spectra is also shown (*open triangles*). The solid line indicates the density profile obtained from the β-parameters derived by fitting the surface brightness profile over the 50–1000 kpc. See text for details.

mass fraction, and $\Lambda(T)$ is the cooling function. We calculate the electron density by following the procedure described in § 6.2, using the β-parameters derived by fitting the surface brightness profile over the 50–1000 kpc region[10] (data in this region can be

[10] The best fit obtained in § 3.1 cannot be extrapolated to the central region ($r \lesssim 100$ kpc) and therefore cannot be used here for the purpose of calculating the central cooling time.

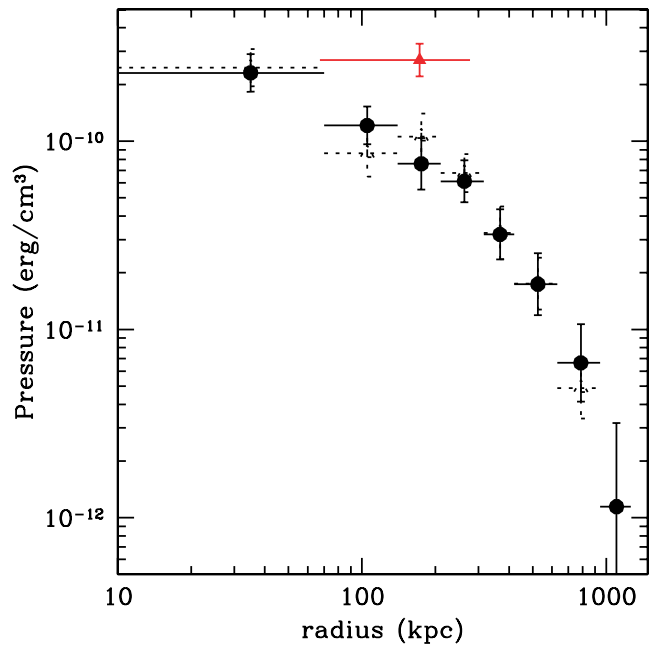

FIG. 10.—X-ray gas pressure profile measured from pn spectra (*filled circles*). For comparison, the profile measured from MOS1+MOS2 spectra is also shown (*open triangles*). The red triangle represents the pressure of the thermal plasma filling the northern cavity, as estimated in § 5.5.

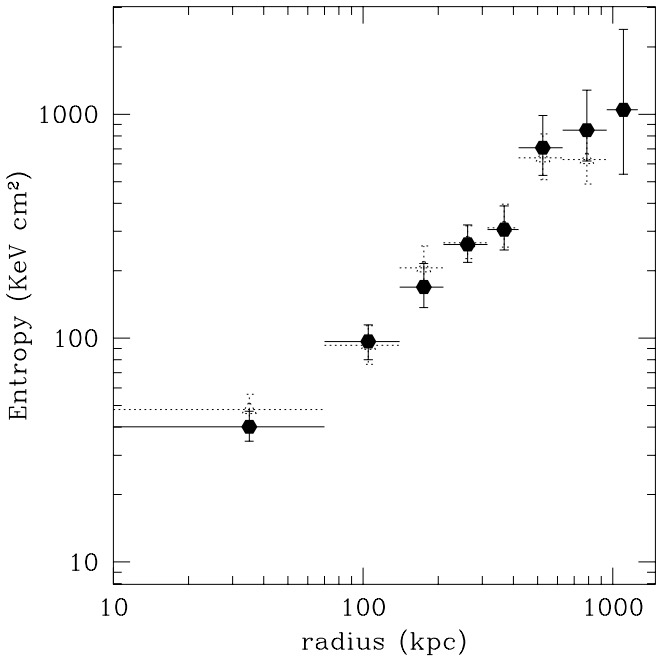

FIG. 11.—X-ray gas entropy profile measured from pn spectra (*filled circles*). For comparison, the profile measured from MOS1+MOS2 spectra is also shown (*open triangles*).

approximated by a β-model with $r_c \sim 150$ kpc and a slope parameter $\beta \sim 0.70$). We note that in the radial range where the β-model is a good representation of the observed surface brightness profile, the density profile derived from this method agrees with that derived from the deprojection analysis of spectra extracted in concentric annuli (see Fig. 9).

Following Bîrzan et al. (2004), we define the cooling radius as the radius within which the gas has a cooling time less than 7.7×10^9 yr, the look-back time to $z = 1$ for our adopted cosmology. With this definition, we find $r_{\rm cool} \sim 100$ kpc, which corresponds to the central 30″. The accumulated spectrum within this radius is extracted and compared to three different spectral models. Model A is the `mekal` model already used in § 5.1. Model B includes a single temperature component plus an isobaric multiphase component (`mekal+mkcflow` in XSPEC), where the minimum temperature, $kT_{\rm low}$, and the normalization of the multiphase component, $\mathrm{Norm}_{\rm low} = \dot{M}$, are additional free parameters. This model differs from the standard cooling flow model as the minimum temperature is not set to zero. Finally, in model C the constant pressure cooling flow is replaced by a second isothermal emission component (`mekal+mekal` in XSPEC). As for model B, this model has two additional free parameters with respect to model A: the temperature, $kT_{\rm low}$, and the normalization, $\mathrm{Norm}_{\rm low}$, of the second component.

The results, summarized in Table 3, show that the statistical improvements obtained by introducing an additional emission component (models B or C) compared to the single-temperature model (model A) are significant at more than the 99% level according to the F-test. With our data, however, we cannot distinguish between the two multiphase models. This means that the extra emission component can be equally well modeled either as a cooling flow or a second isothermal emission component. We note that the fit with the modified cooling flow model sets tight constraints on the existence of a "pedestal" minimum temperature (~1.5 keV). The nominal mass deposition rate in this empirical model is $\sim 260 \pm 30\ M_\odot\ \mathrm{yr}^{-1}$. We also attempt the fit with a classical cooling flow model (model D), by

TABLE 3
Cooling Flow Analysis

Parameter	Model A	Model B	Model C	Model D
kT	$3.87^{+0.09}_{-0.09}$	$7.61^{+0.45}_{-1.28}$	$6.07^{+1.27}_{-0.63}$	$4.25^{+0.15}_{-0.18}$
Z	$0.57^{+0.05}_{-0.05}$	$0.52^{+0.06}_{-0.05}$	$0.52^{+0.05}_{-0.06}$	$0.59^{+0.05}_{-0.05}$
Norm	1.7×10^{-3}	7.9×10^{-5}	9.1×10^{-4}	1.4×10^{-3}
$kT_{\rm low}$	...	$1.45^{+0.23}_{-0.14}$	$2.27^{+0.41}_{-0.39}$	0.1
$\rm Norm_{low}$	...	$\dot{M} = 260$	6.7×10^{-4}	$\dot{M} = 40$
χ^2/dof	891/787	839/785	839/785	861/786

Notes.—The best-fit parameter values and 90% confidence limits of the spectral analysis in the central 30″ region. Temperatures (kT) are in keV, metallicities (Z) as a fraction of the solar value and normalizations in units of $10^{-14} n_e n_p V / 4\pi[D_A(1+z)]^2$ as done in XSPEC (for the `mkcflow` model the normalization is parameterized in terms of the mass deposition rate $\dot{M}$, in $M_\odot$ yr^{-1}). See text for details.

imposing $kT_{\rm low} = 0.1$ keV, and find a mass deposition rate $\dot{M} \sim 40 \pm 10\ M_\odot\ {\rm yr}^{-1}$.

5.5. *Cavity Regions*

Several states of matter have been proposed to fill the cavities (Pfrommer et al. 2005), including a population of relativistic electrons radiating at low radio frequencies and a dilute, shock-heated thermal gas. The synchrotron emission from radio-filled cavities provides evidence of the existence of relativistic electrons and magnetic fields. The cavities may also be filled with a shock-heated thermal gas that can contribute to their internal pressure. This possibility is strengthened if the assumption of equipartition holds. Indeed, since the equipartition estimates of the nonthermal pressure in the radio bubbles give values which are typically a factor of 10 smaller than the thermal pressures of the surrounding X-ray gas (e.g., Blanton et al. 2001; De Young 2006), the fact that the cavities are long-lived indicates that the necessary pressure support might be supplied by an additional thermal component. Observationally, besides the detection of hot X-ray-emitting gas claimed by Mazzotta et al. (2002) within the ghost cavity of the MKW3s cluster, there has been no detection of hot gas over the cavities even in the clusters with better data available.

In the case of MS 0735, the existence of a relativistic plasma filling the cavities is clearly indicated by the presence of the radio source at the position coincident with the holes in the X-ray emission (McNamara et al. 2005). In order to investigate the possibility of an additional thermal gas component in the cavities, we perform a detailed analysis by modeling the spectra extracted in the cavity regions as the sum of ambient cluster emission and a hot thermal plasma, each with a characteristic temperature. The northern and southern cavity regions, detailed in Figure 12, contain 10,083 and 8872 source counts with a count rate of 0.23 and 0.20 counts s^{-1} (MOS+pn), respectively. The results of the spectral analysis are reported in Table 4.

In the northern cavity, which shows a higher brightness contrast than the southern one in the *XMM* image, we find indications of the presence of a ~13 keV plasma. By assuming that the emission of this hottest component comes entirely from the cavity region whereas that of the coolest component is due to the projected foreground and background cluster emission,[11] we can estimate the density of the thermal plasma in the cavity to be $n_e \sim 6.4 \times 10^{-3}$ cm^{-3}. This result leads to an estimate of its pressure of

[11] This assumption is justified by the fact that a component as hot as 13 keV is detected nowhere else in the cluster and therefore is plausibly located only in the cavity region.

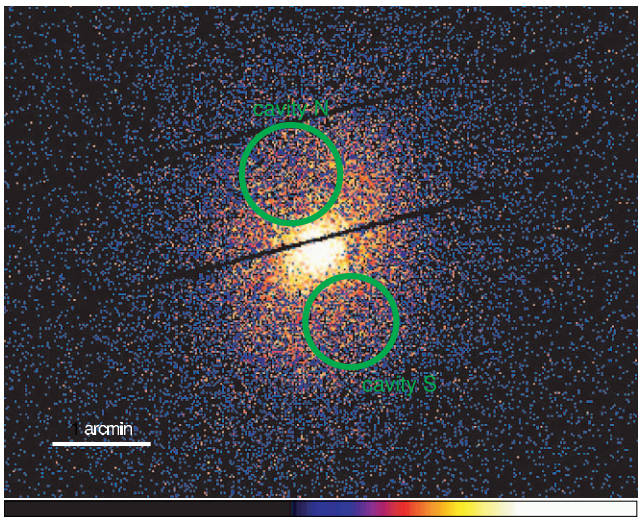

Fig. 12.—Regions considered for the spectral analysis of the cavities. The N and S cavities have a radius of 105 kpc and are located at a distance of ~170 and ~180 kpc from the cluster center, respectively.

$\sim 2.7 \times 10^{-10}$ ergs cm^{-3}, which is a factor ~3–4 higher than the pressure of the surrounding medium (see Fig. 10).

However, we note that the improvement in the fit due to the extra thermal component is only marginally significant.[12] We therefore cannot place strong constraints on the existence of a hot thermal component filling the cavities and the estimate presented above has to be considered with caution.

5.6. *Shock Front*

A *Chandra* observation of MS 0735 reveals a discontinuity in the X-ray surface brightness that has been interpreted as a weak cocoon shock driven by the expansion of the radio lobes that inflate the cavities. The shock front has an elliptical shape, being located ~240 and ~360 kpc from the cluster center in east-west and north-south directions, respectively (McNamara et al. 2005). We find indications of a surface brightness feature at a position consistent with that seen in the *Chandra* data, however we cannot

[12] The fit with the extra thermal component gives a value χ^2/dof = 385/311 compared to χ^2/dof = 394/313, with F-test probability = 0.028.

TABLE 4
Cavity Analysis

Cavity	Parameter	`mekal`	`mekal+mekal`
N	kT_1	$5.24^{+0.36}_{-0.33}$	$13.1^{+27.6}_{-4.7}$
	Z	$0.31^{+0.12}_{-0.11}$	$0.28^{+0.13}_{-0.12}$
	$\rm Norm_1$	4.9×10^{-4}	2.3×10^{-4}
	kT_2	...	$3.45^{+0.96}_{-1.00}$
	$\rm Norm_2$	...	2.7×10^{-4}
	χ^2/dof	394/313	385/311
S	kT_1	$5.00^{+0.36}_{-0.33}$	$0.43^{+0.21}_{-0.15}$
	Z	$0.28^{+0.12}_{-0.11}$	$0.28^{+0.14}_{-0.10}$
	$\rm Norm_1$	3.9×10^{-4}	...
	kT_2	...	$5.31^{+0.41}_{-0.36}$
	$\rm Norm_2$	...	3.8×10^{-4}
	χ^2/dof	288/287	275/285

Notes.—The best-fit parameter values and 90% confidence limits of the spectral analysis in the cavity region. Temperatures (kT) are in keV, metallicities (Z) as a fraction of the solar value and normalizations in units of $10^{-14} n_e n_p V / 4\pi[D_A(1+z)]^2$ as done in XSPEC.

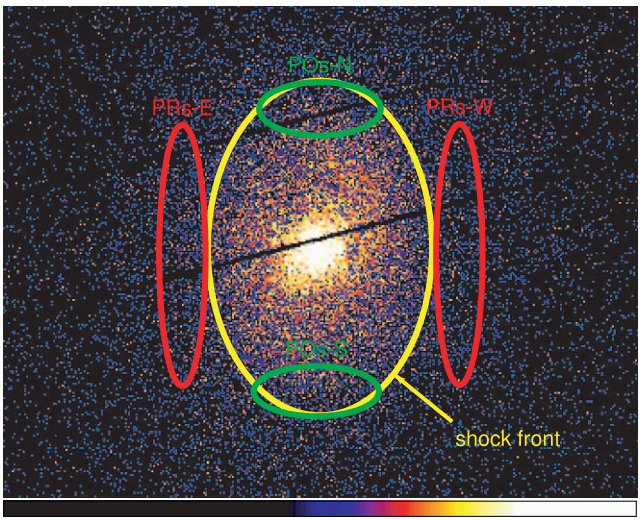

FIG. 13.—Elliptical regions considered for the spectral analysis of the preshock and postshock gas. The centers of the ellipses are chosen to be at the same radial distance from the cluster center (~300 kpc), in order to allow us to make a direct comparison of the spectral properties in different directions with respect to the azimuthally averaged profiles (see Figs. 15 and 27).

clearly distinguish a break in surface brightness that would be a signature of the shock front. By considering the elliptical shock front position derived from *Chandra* data, we perform a spectral analysis on the regions detailed in Figures 13 and 14 in order to derive the temperature of the preshock and postshock gas. The results are reported in Table 5.

The particular choice of the elliptical regions next to specific sectors of the shock front (see Fig. 13) allows us to compare directly the spectral properties of the preshock and postshock regions in different directions with respect to the azimuthally averaged profiles. We do not find any appreciable variation in temperature (see Fig. 15). In the analysis of the *Chandra* data, the shock properties are determined using a spherical hydrodynamic model of a point explosion at the center of an initially isothermal, hydrostatic atmosphere. When adapted to the *XMM* data by taking into account the smearing effect due to the large PSF, such a model

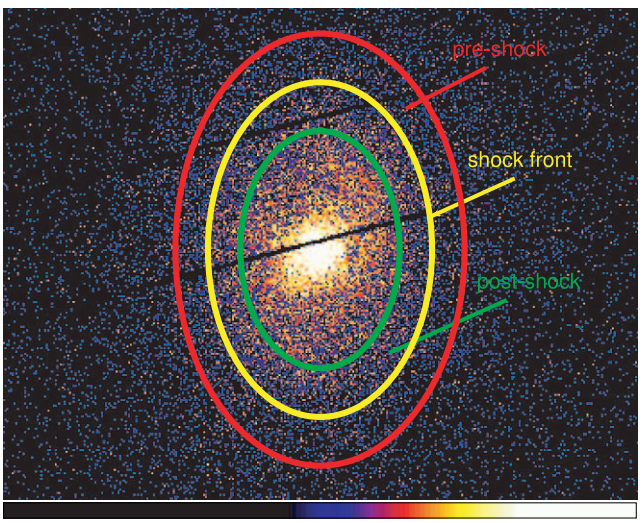

FIG. 14.—Elliptical regions considered for the spectral analysis of the preshock and postshock gas. The concentric annular regions are defined in order to surround the whole shock front as derived from the *Chandra* data.

TABLE 5
SHOCK ANALYSIS

Region	Source Counts (MOS+pn)	kT (keV)	Z ($Z_\odot$)	χ^2/dof
PRs-E	3081	$6.15^{+1.25}_{-0.88}$	$0.34^{+0.33}_{-0.29}$	143/122
PRs-W	2361	$4.82^{+0.71}_{-0.56}$	$0.44^{+0.36}_{-0.30}$	87/100
POs-N	2958	$5.29^{+0.72}_{-0.62}$	$0.27^{+0.26}_{-0.22}$	116/110
POs-S	3122	$5.57^{+0.94}_{-0.74}$	$0.25^{+0.26}_{-0.24}$	113/118
(PRs-E)+(PRs-W)	5442	$5.34^{+0.58}_{-0.50}$	$0.42^{+0.23}_{-0.20}$	301/227
(POs-N)+(POs-S)	6080	$5.43^{+0.60}_{-0.46}$	$0.25^{+0.17}_{-0.16}$	233/233
PRs (annulus)	13187	$5.24^{+0.36}_{-0.33}$	$0.21^{+0.10}_{-0.09}$	440/461
POs (annulus)	22655	$5.63^{+0.26}_{-0.24}$	$0.29^{+0.07}_{-0.07}$	647/634

NOTES.—Results from the spectral fitting in the regions indicated in Figs. 13 and 14. The fit is performed in the [0.4–10.0] keV energy range by fixing the absorbing column density to the Galactic value. When fitting simultaneously two different regions at the same radial distance from the center (e.g., PRs-E+PRs-W), the normalizations of each camera are linked in order to have the same value in the two regions. Error bars are at the 90% confidence levels on a single parameter of interest.

predicts a temperature rise of ~10% (see Fig. 16). Our spectral results obtained from elliptical annular regions next to the whole shock front (see Fig. 14) do suggest a temperature jump at the shock front, in agreement with those derived from previous *Chandra* observations, although due to the large error bars the preshock and postshock regions are still consistent with being isothermal (see Fig. 17).

From this analysis we therefore conclude that the *XMM* data can neither confirm or deny the existence of the shock front.

6. MASS PROFILE

6.1. *Total Gravitational Mass*

In the following we estimate the total mass of the cluster using the usual assumptions of hydrostatic equilibrium and spherical

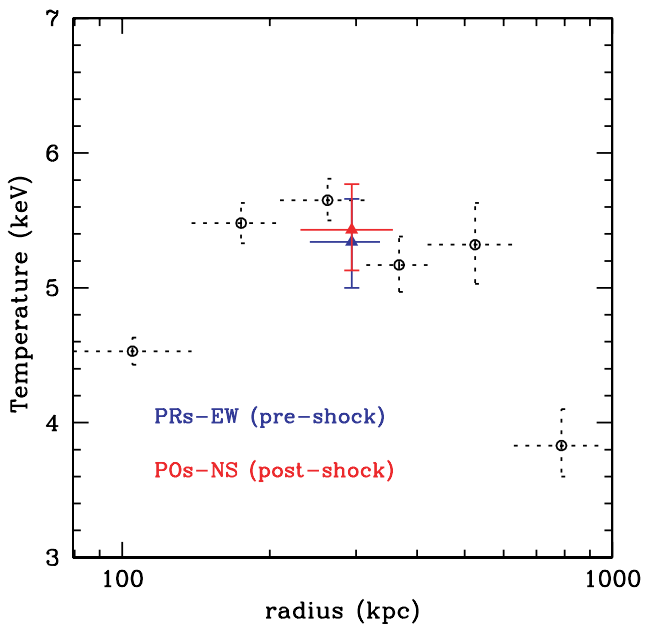

FIG. 15.—Open circles represent the projected temperature profile measured in § 5.2. The blue triangles indicate the measurements in the preshock regions along the east-west direction, the red square indicate the measurements in the postshock regions along the north-south direction (see Fig. 13). The error bars are at 1 σ level.

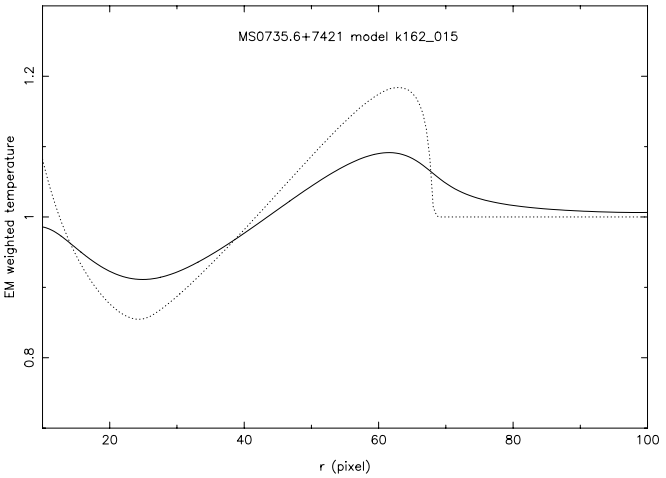

FIG. 16.—Temperature jump expected by the shock model. The dotted line shows the projected temperature profile as it would be seen by *Chandra*, and the full line is the result after smearing with the *XMM* PSF. The temperatures are in units of the preshock temperature, assumed to be constant. The radial distance is in *Chandra* pixel unit (1 pixel = 0.492″).

symmetry. Under these assumptions, the gravitational mass $M_{\rm tot}$ of a galaxy cluster can be written as:

$$M_{\rm tot}(<r) = -\frac{kTr}{G\mu m_p}\left(\frac{d\ln n_g}{d\ln r} + \frac{d\ln T}{d\ln r}\right), \qquad (2)$$

where G and m_p are the gravitational constant and proton mass and $\mu \approx 0.61$. The mass contribution from galaxies is small, and thus we neglect it. Therefore, $M_{\rm tot}(<r) = M_{\rm gas}(<r) + M_{\rm DM}(<r)$, i.e., the total gravitational mass within a sphere of radius r is given by gas plus dark matter mass.

The mass profile derived from the equilibrium equation is strongly dependent on the measured temperature profile. Large errors and irregular radial distribution of the temperature values induce large scatter on the reconstructed gravitational mass measurements. In order to obtain reliable mass estimates it is therefore crucial to select bins with a robust temperature estimate. For this reason we exclude the last temperature bin, although its inclusion would allow us to trace the temperature profile and therefore mass profile at much larger radii.

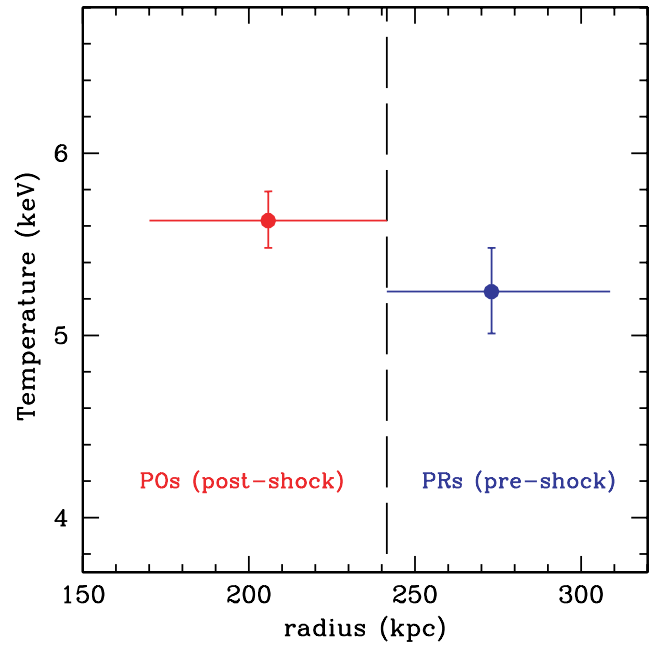

FIG. 17.—Temperature measured in the annular preshock (*blue*) and postshock (*red*) regions (see Fig. 14). The dashed line represents the position of the shock front along the east-west direction. The error bars are at 1 σ level.

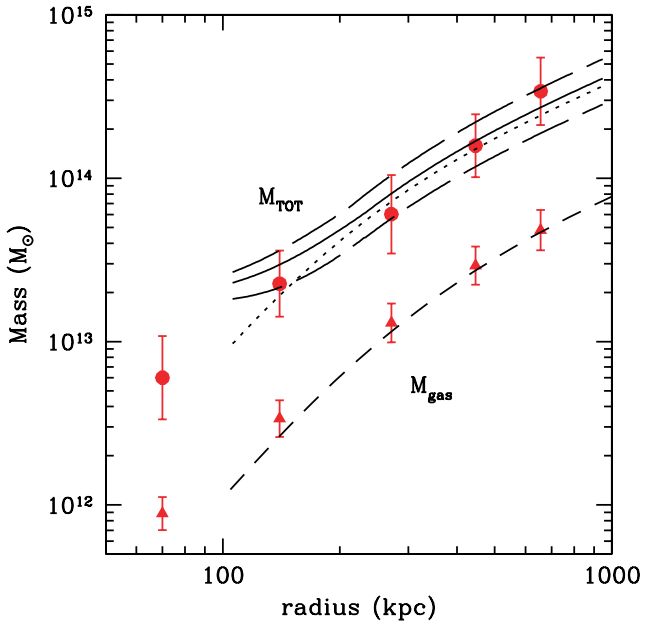

FIG. 18.—Mass profiles calculated with different methods. *Red circles*: Total mass profile derived from deprojected gas temperature and density values. *Black solid line*: Total mass calculated from eq. (4) by estimating the temperature gradient from the deprojected temperature profile (with error on the mass calculation coming from the temperature measurement and β-model, *shown by the black long dashed lines*). *Black dotted line*: Total mass calculated from eq. (4) by assuming a constant temperature of 4.79 keV. *Red triangles*: Gas mass profile derived from deprojected analysis. *Black dashed line*: Gas mass profile derived from β-model fit. See text for details.

The deprojected $d\ln n_g/d\ln r$ is calculated from the parameters of the β-model derived in § 3.1. In particular, the advantage of using a β-model to parameterize the observed surface brightness is that gas density and total mass profiles can be recovered analytically and expressed by simple formulae:

$$n_{\rm gas}(r) = n_{0,\rm gas}\left[1+\left(\frac{r}{r_c}\right)^2\right]^{-3\beta/2}, \qquad (3)$$

$$M_{\rm tot}(<r) = \frac{kr^2}{G\mu m_p}\left(\frac{3\beta rT}{r^2+r_c^2} - \frac{dT}{dr}\right). \qquad (4)$$

As a first-order approximation, the temperature gradient is estimated by dividing the deprojected temperature profile (see Fig. 7) into two radial intervals and least-squares fitting a straight line in each interval. The total gravitating mass distribution derived from equation (4) is shown in Figure 18 as a solid line, with errors coming from uncertainties in the temperature measurement and β-model parameters represented as long dashed lines. In Figure 18 we also show (dotted line) the total mass calculated by assuming a constant temperature of $\langle T_{\rm X}\rangle = 4.79$ keV, where the average emission-weighted cluster temperature $\langle T_{\rm X}\rangle$ is derived by extracting the global spectrum of the cluster after excluding the cooling flow region (i.e., in the annular region 30″–6′). We note that the total integrated mass within a particular volume is dependent on the local physical properties (local temperature and

density gradients) and is not strongly affected by the regions interior, or exterior, to that radius. The mass profile derived with this method is thus reliable in the region where the β-model is a good representation of the observed surface brightness profile (100 kpc $\lesssim r \lesssim$ 1150 kpc; see § 3.1), whereas it cannot be extrapolated to the central region.

As an alternative method, we then calculate the total mass by making direct use of the deprojected gas temperature and electron density values estimated from the spectral best-fit with a single phase model (§ 5.3). In particular, the total mass enclosed within the midpoint between two consecutive shells is calculated from the pressure gradient and the gas density at the midpoint by following the method described in Voigt & Fabian (2006). The mass profile reconstructed by using this method, is shown as full red circles in Figure 18. The uncertainties are calculated using error propagation from the pressure and density estimates (90% confidence level). We note that the cavities may affect the mass determination. In particular, since the cluster does not exhibit a smooth pressure profile between 100–400 kpc (see Fig. 10), which would result in a nonmonotonically increasing mass profile in this region, we exclude the fourth data point in the pressure and gas density profiles.

The mass measurements reconstructed through the two different methods (direct application of the hydrostatic equilibrium equation with density profile derived from either β-model fit to the surface brightness profile or deprojection analysis on annular spectra) are in very good agreement (see also Fig. 20).

6.2. *Gas Mass and Gas Mass Fraction*

We estimate the gas mass through two different methods, i.e., by using the density profile derived from either the β-model fit to the surface brightness profile or the deprojection analysis on annular spectra. To convert from electron number density to gas density we use the relation $\rho = 1.83\mu m_{\rm H} n_e$.

In the first case, the gas mass profile is derived by integrating the gas density given by equation (3) in spherical shells and using the β-model parameters determined in § 3.1. The normalization of equation (3) is obtained from the combination of the best-fit results from the spectral and imaging analyses, which allows us to determine the conversion count rate flux used to derive the bremsstrahlung emissivity that is then integrated along the line-of-sight and compared with the central surface brightness value. The adoption of the parameters of the β-model fit in the outer regions produces an underestimate of the derived central electron density (see Fig. 9), and this turns into an underestimate of the gas mass in the central shells. Since the integrated gas mass is calculated by summing from the center outward, any error in the measurement at small radii will propagate out to larger radii. However, the gas mass at small radii is much less than at large radii and any uncertainty in the measurements in the core are unlikely to have a significant effect on the gas mass profile further out. The gas mass profile derived from the β-model is shown as a dashed line in Figure 18. The gas mass profile obtained by integrating in spherical shells the gas density derived directly from the deprojected electron number density is shown in Figure 18 as red triangles. Again we note that the two profiles are in very good agreement.

The gas mass fraction is the ratio of the total gas mass to the total gravitating mass within a fixed volume:

$$f_{\rm gas}(r) = \frac{M_{\rm gas}(<r)}{M_{\rm tot}(<r)}. \quad (5)$$

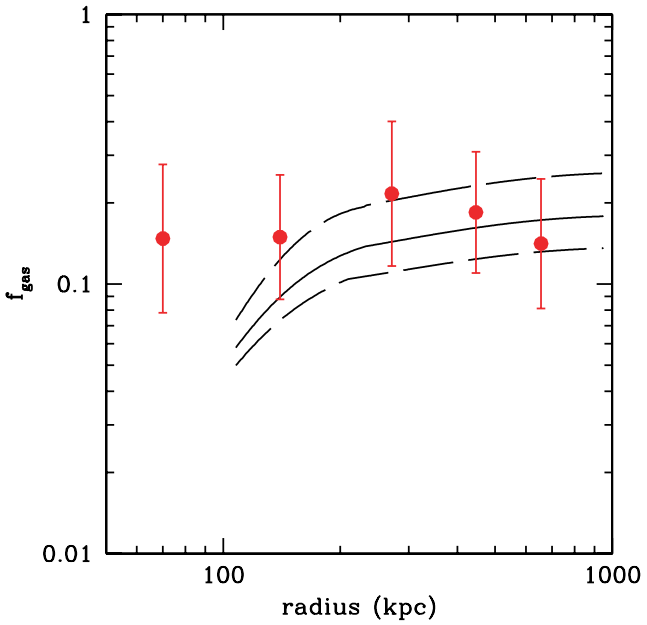

FIG. 19.—The $f_{\rm gas}$ profile derived with different methods. *Red circles*: $f_{\rm gas}$ profile derived from $M_{\rm tot}$ and $M_{\rm gas}$ measured directly from the deprojected density and temperature values (see Fig. 18, *red circles and red triangles*). *Black solid line*: $f_{\rm gas}$ profile (*with error shown by the black long dashed lines*) derived from $M_{\rm tot}$ and $M_{\rm gas}$ measured by using the density profile derived from the β-model fit to the surface brightness profile (see Fig. 18, *black solid line and black dashed line*).

The gas mass fraction profile derived from $M_{\rm tot}$ and $M_{\rm gas}$ measured from the β-model and deprojection methods are plotted in Figure 19 as black lines and red points, respectively. Adding the mass contribution from galaxies ($\sim$1%–2%; Lin et al. 2003) to the total mass would have a small effect on the estimate of $f_{\rm gas}$, with variations lying within the error bars.

7. DISCUSSION

Simple assumptions for the formation and evolution of galaxy clusters predict self-similar scaling relations. Galaxy clusters are assumed to form by spherical collapse of dark matter and gas due to gravitational instability. The gas is heated by shocks and adiabatic compression. For dissipationless collapse, the X-ray emitting gas can be considered to share the same properties as the dark matter (e.g., Bryan & Norman 1998; Arnaud & Evrard 1999). Self-similar dark matter halos are assumed to have identical properties when scaled by the virial radius, which is the radius separating the region where the cluster is in hydrostatic equilibrium from where matter is still infalling. However, deviations from self-similarity are expected in the ICM due to the details of individual collapse histories and to any physical processes beyond simple gravity and gas dynamics (e.g., Evrard & Henry 1991; Bryan & Norman 1998; Borgani et al. 2002, and references therein). In particular, the ICM of cooling flow clusters is affected significantly by heating that boosts the thermal energy of the gas.

Here we investigate the correlations between the physical quantities observed for MS 0735 in order to scale it in the overall populations of clusters and assess its conformity to the generally observed mass-temperature (M-T) and luminosity-temperature (L-T) relations. Our final aim is to evaluate the impact of energetic AGN outbursts on such scaling relations, which are the foundation to construct the cluster mass function and to use these virialized objects as cosmological probes.

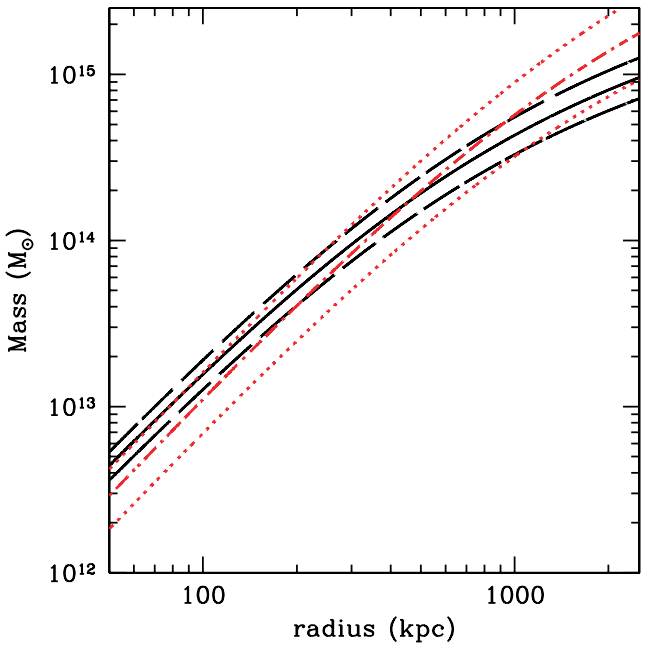

FIG. 20.—Best fits of the NFW mass profile calculated with different methods. *Red dashed-dotted line*: Best-fit NFW to the total mass profile measured from the deprojected density and temperature values, with 1 σ error shown by the red dotted lines. *Black solid line*: Best-fit NFW to the total mass profile measured from the density profile derived from the β-model fit to the surface brightness profile, with 1 σ error shown by the black long dashed lines.

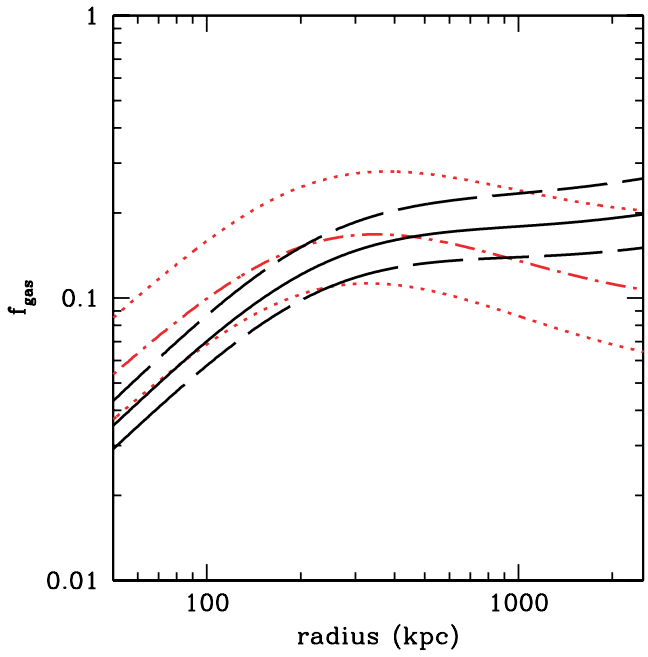

FIG. 21.—The f_{gas} profile estimated from the NFW total mass profile derived with different methods (the gas mass is estimated from the β-model fit to the surface brightness profile). The line colors and styles are the same as in Fig. 20.

7.1. *Modeling the Observed Mass Profile: Determination of r_Δ*

In order to rank MS 0735 in the overall population of clusters we investigate the relations among different physical quantities considering their values at a given overdensity Δ. This is defined with respect to the critical density $\rho_{c,z} = (3H_z^2)/(8\pi G)$, and within a cluster described as a sphere with radius r_Δ:

$$\Delta = \frac{3M_{\rm tot}(<r_\Delta)}{4\pi\rho_{c,z}r_\Delta^3}, \tag{6}$$

where the Hubble constant at redshift z is equal to (e.g., Bryan & Norman 1998):

$$H_z = H_0\sqrt{\Omega_m(1+z)^3+1-\Omega_m} \equiv H_0\ h(z). \tag{7}$$

In order to estimate r_Δ for various overdensities we need to fit the mass profile with an analytical function, which allows us to extrapolate the mass profile beyond the outer radius accessible to our X-ray observations. As a cosmologically motivated dark matter mass model, we consider the integrated Navarro-Frenk-White (NFW; Navarro et al. 1996) dark matter profile:

$$M_{\rm DM}(<r) = 4\pi r_s^3\rho_{c,z}\frac{200}{3}\frac{c^3\{\ln(1+r/r_s)-[(r/r_s)/(1+r/r_s)]\}}{\ln(1+c)-c/(1+c)}. \tag{8}$$

The scale radius r_s and the concentration parameter c are the free parameters.

We perform the fit to minimize the χ^2 of the comparison between the mass predicted by equation (8) and the mass profile reconstructed from both the density profiles estimated from the β-model and deprojection methods. The best-fit parameters for the mass profile reconstructed from density values estimated from the β-model are $r_s = 498^{+36}_{-38}$ kpc, $c = 3.45^{+0.18}_{-0.19}$ (χ^2/dof = 0.08/4). The best-fit parameters for the mass profile reconstructed from deprojected density values are: $r_s = 1343^{+235}_{-240}$ kpc, $c = 1.66^{+0.18}_{-0.21}$ (χ^2/dof = 0.18/3). The quoted errors are at the 68% confidence levels (1 σ). The comparison of the two best fits of the NFW mass profile is shown in Figure 20. The corresponding gas mass fraction estimated from the NFW mass profile fit is shown in Figure 21 for both the β-model and deprojection methods. Note that we neglect the gas mass contribution to the total mass and we assume $M_{\rm tot}(<r) = M_{\rm DM}(<r)$. We also perform the same fitting procedure by including the gas mass, i.e., by assuming $M_{\rm tot}(<r) = M_{\rm DM}(<r) + M_{\rm gas}(<r)$, and find very similar results.

From the best-fit parameters we compute r_Δ from equation (6) for various overdensities: $\Delta = 2500, 1000, 500, 200$. For $\Omega_m + \Omega_\Lambda = 1$, the virial radius corresponds to r_Δ if $\Delta = \Delta_{\rm vir} = 178\Omega_m^{0.45}$ (Lacey & Cole 1993; Eke et al. 1996, 1998). For $\Omega_m = 0.3$ adopted here, $\Delta_{\rm vir} = 104$. The virial radius derived in an Einstein-de Sitter universe ($\Omega_m = 1$) is still often used in the literature, corresponding to a density contrast of $\Delta_{\rm vir} = 178$ (or $\Delta_{\rm vir} = 200$), so that $r_{\rm vir} \sim r_{200}$. The relation $r_{\rm vir} = c \times r_s$ holds for the NFW mass profile. The results obtained from the NFW fit to the mass estimated through the β-model and deprojection methods are shown in the Tables 6 and 7, respectively. We also report the total mass and the gas mas fraction. The error related to the mass estimate is obtained from half the difference between the maximum and the minimum value calculated at each radius for the set of parameters acceptable at 1 σ. The gas mass fraction is calculated at given overdensities by adopting the gas mass computed from the integration of the β-model fit to the density profile extrapolated out to r_Δ. The reported error is obtained from the error propagation and is dominated by the error on the total mass.

We note that the value obtained for r_{200} is highly dependent on the accuracy of r_s, since it involves extrapolating the NFW model using r_s. The measure of r_s is very uncertain, as the best-fit scale radius lies beyond the radius at which mass measurement can be made and is therefore strongly dependent on the outermost data point of the mass profile. The value for r_{200} is shown

TABLE 6
RESULTS FROM β-MODEL ANALYSIS

Δ	r_Δ (kpc)	$M_{\rm tot}$ ($10^{14}\ M_\odot$)	$f_{\rm gas}$
200	1718 (218)	7.12 (1.96)	0.188 (0.052)
500	1107 (145)	4.77 (1.26)	0.181 (0.048)
1000	775 (105)	3.27 (0.83)	0.176 (0.046)
2500	463 (65)	1.74 (0.42)	0.165 (0.040)

NOTES.—Characteristic radii r_Δ, total mass $M_{\rm tot}$, and mass gas fraction $f_{\rm gas}$ for various overdensities Δ derived from the NFW fit to the mass estimated through the β-model. All the quantities are estimated within r_Δ (1 σ errors in parentheses).

for interest but is not used for any subsequent analysis. We instead adopt r_{2500}, which is the most reliable estimate, since it lies well within the radius at which mass measurements are obtained. We indeed find an excellent agreement between the values of r_{2500}, M_{2500} and $f_{\rm gas,2500}$ obtained from the NFW fit to the mass estimated through the β-model and deprojection methods. In particular, in the following discussion we adopt the values obtained with the β-model method as their determination is more precise (see Tables 6 and 7).

The gas mass fraction profile scaled in radial units of r_{2500} is shown in Figure 22. The apparent flattening of $f_{\rm gas}$ outside r_{2500} is in agreement with previously observed profiles (Allen et al. 2002; Voigt & Fabian 2006), although it is systematically slightly above them. In particular, we find $f_{\rm gas,2500} = 0.165 \pm 0.040$, which is higher than the average value derived in a number of previous measurements with *Chandra* (e.g., Allen et al. 2002; Vikhlinin et al. 2006). The high central gas fraction is close to the global baryon fraction in the universe, constrained by CMB observations to be $\Omega_b/\Omega_m = 0.175 \pm 0.023$ (Readhead et al. 2004; Spergel et al. 2003). However, our estimate of the central $f_{\rm gas}$ could be affected by several effects. In particular, the high measured central gas mass fraction could result from an underestimation of the total mass, supporting the presence of nonthermal pressure in the core. It could also result from an overestimate of the gas density due to the boost in emissivity produced by the cavities (see § 7.6).

7.2. *Scaled Temperature Profile*

In order to make a fair comparison between the physical properties and investigate the scaling relations it is important to correct for the effects of the central cooling flow when measuring the characteristic temperature of the cluster. The average emission-weighted cluster temperature is calculated by fitting with a `mekal` model the spectrum extracted up to the outer radius detected by our X-ray observation (6′), after excising the cooling region (30″). We find a value $\langle T_{\rm X}\rangle = 4.79 \pm 0.13$ keV.

TABLE 7
RESULTS FROM DEPROJECTION ANALYSIS

Δ	r_Δ (kpc)	$M_{\rm tot}$ ($10^{14}\ M_\odot$)	$f_{\rm gas}$
200	2230 (650)	15.6 (8.78)	0.109 (0.061)
500	1340 (410)	8.46 (4.42)	0.124 (0.065)
1000	875 (280)	4.71 (2.33)	0.141 (0.070)
2500	465 (158)	1.76 (0.81)	0.165 (0.076)

NOTES.—Characteristic radii r_Δ, total mass $M_{\rm tot}$, and mass gas fraction $f_{\rm gas}$ for various overdensities Δ derived from the NFW fit to the mass estimated through the deprojection. All the quantities are estimated within r_Δ (1 σ errors in parentheses).

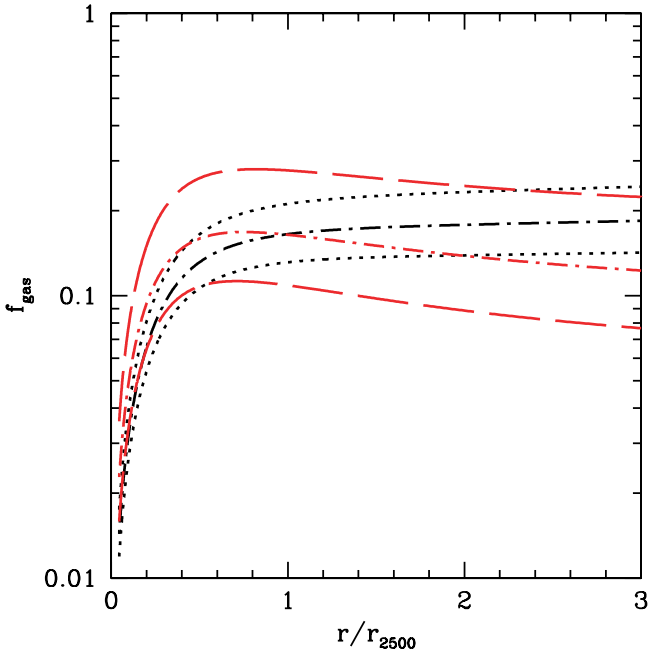

FIG. 22.—The $f_{\rm gas}$ profile with the radial axis scaled in units of r_{2500}. The line colors and styles are the same as in Fig. 20.

We show in Figure 23 the projected temperature profile of MS 0735 (*red triangles*) measured in the region internal to r_{2500}. The profile is scaled at an overdensity of 2500 and overlaid to the scaled temperature profiles of a sample of 6 relaxed clusters observed with *Chandra* (Allen et al. 2001). In Figure 24 we present the same kind of comparison with a sample of 12 relaxed clusters for which the temperature profile has been measured farther out, up to more than $2r_{2500}$, revealing a clear general temperature

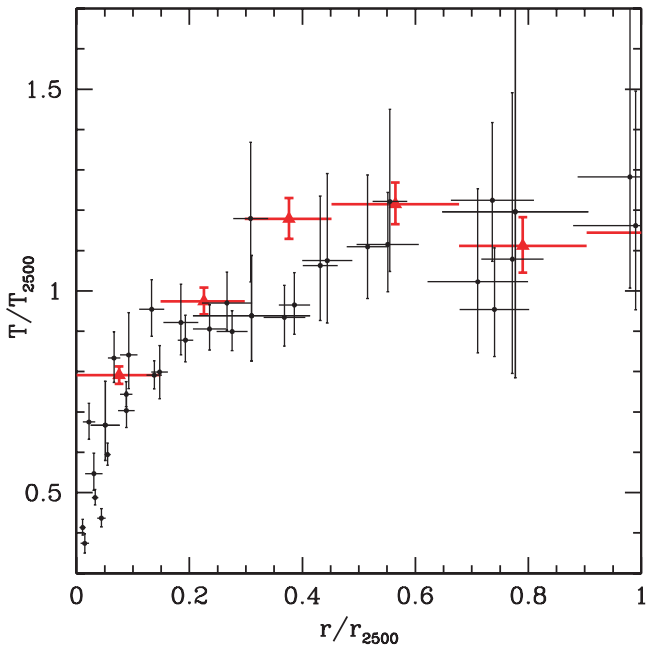

FIG. 23.—Temperature profile measured for MS 0735 (*red triangles*) overlaid onto the temperature profile observed for a sample of six relaxed clusters presented by Allen et al. (2001). The profiles for all clusters are projected and scaled in units of T_{2500} and r_{2500}. T_{2500} is estimated within r_{2500} and results $T_{2500} = 4.65 \pm 0.08$ keV for MS 0735.

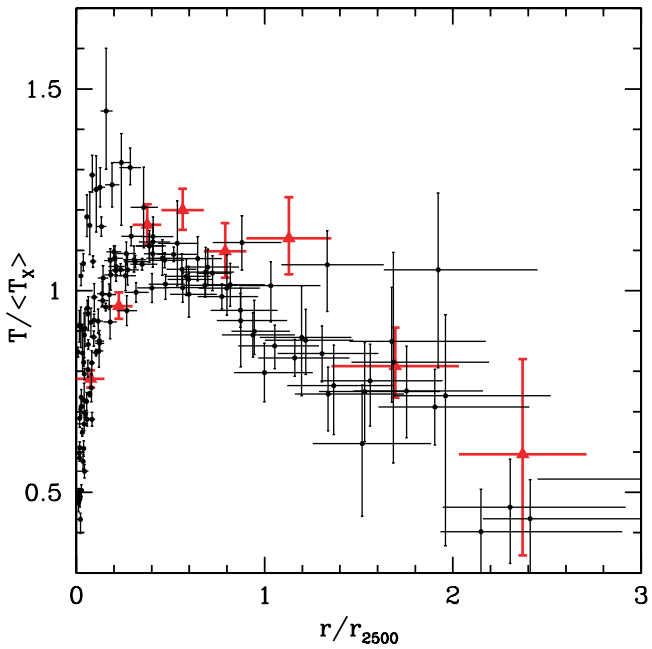

FIG. 24.—Temperature profile measured for MS 0735 (*red triangles*) overlaid onto the temperature profile observed for a sample of 12 relaxed clusters presented by Vikhlinin et al. (2005). The profiles for all clusters are projected and scaled in radial units of r_{2500}. The temperatures are scaled to the cluster emission-weighted temperature excluding the central 70 kpc regions.

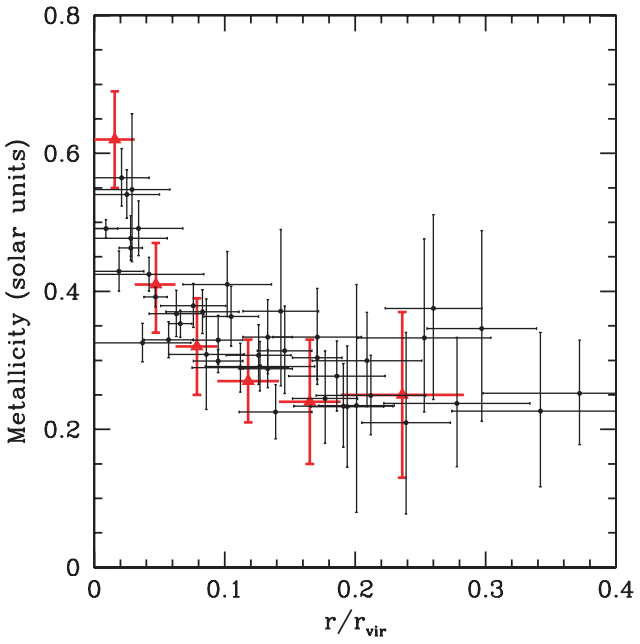

FIG. 25.—Metallicity profile measured for MS 0735 (*red triangles*) overlaid onto the metallicity profile observed for a sample of nine cooling flow clusters presented by De Grandi & Molendi (2001). The profiles for all clusters are projected and scaled in radial units of r_{vir}. The virial radius is estimated from the relation $r_{vir} = 3.95$ Mpc $(\langle T_X \rangle/10 \text{ keV})^{1/2}$ (Evrard et al. 1996; see also § 7.4). $H_0 = 50$ km s^{-1} Mpc^{-1}, $\Omega = 1$, and $\Lambda = 0$ are assumed.

decline in the outer regions (Vikhlinin et al. 2005). In this case the temperatures are scaled to the emission-weighted cluster temperature, excluding the central 70 kpc region usually affected by radiative cooling. To be fully consistent with the scaled profiles presented by Vikhlinin et al. (2005), we thus estimate the emission-weighted temperature used for the scaling by extracting the global spectrum of MS 0735 in the annular region $20''$–$6'$. We find a value ($kT = 4.71 \pm 0.11$ keV) slightly lower than the "true" average emission-weighted temperature, as expected since the effect of cooling flow is not completely corrected (the cooling radius in MS 0735 is $\sim$100 kpc). The overall temperature profile measured for MS 0735 is consistent within the scatter of the profiles observed in relaxed cluster, although for $r > 0.5r_{2500}$ its values tend to lie at the top of the distribution.

These results indicate that the energetic outburst in MS 0735 does not cause dramatic instantaneous departures from the average properties of the ICM, as it has not had a large impact on the large-scale temperature profile. Of the roughly 30 clusters from the *Chandra* archive showing evidence of AGN outbursts (Rafferty et al. 2006), three have outbursts of comparable energy, MS 0735 (McNamara et al. 2005), Hercules A (Nulsen et al. 2005a), and Hydra A (Nulsen et al. 2005b; Wise et al. 2007). These three large outbursts all have ages of $\sim 10^8$ yr. Dunn et al. (2005) find that $\sim$70% of cooling flow clusters currently show signs of outbursts, implying that outbursts are active most of the time. If the large outbursts were confined to only these few clusters, their incidence and ages imply that the clusters have undergone tens of outbursts since they were formed. In that case, the total energy added to the ICM outside the cooling region should have had a marked effect, contradicting our findings for MS 0735. Thus, the relatively high incidence of large outbursts is more likely to be due to them occurring $\sim$10% of the time in a significant proportion of all cooling flow clusters, rather than occurring most of the time in $\sim$10% of clusters.

7.3. *Scaled Metallicity Profile*

We studied the metallicity profile in order to investigate the possible effect of uplifting and outflows on the metal distribution. Figure 25 shows the projected metallicity profile of nine cooling flow clusters observed with *BeppoSAX*, rescaled to the virial radius (De Grandi & Molendi 2001). A strong enhancement in the abundance is found in the central regions. Overlaid is the metallicity profile that we measure for MS 0735 (*red triangles*). We note that it is fully consistent with the strong central enhancement in the abundance exhibited by cooling flow clusters, indicating that the outburst has not smoothed the metal gradient.

How to interpret this result in the context of current models is unclear. Simulations of metal evolution due to mixing and uplifting by buoyant bubbles indicate that low-power, subsonic flows have a relatively weak impact on the metallicity gradients found in clusters (Brüggen 2002; Omma et al. 2004), whereas powerful outbursts with short active time can flatten the central metallicity gradients if the metals are not replenished quickly (Heath et al. 2007). The average jet power of the outburst in MS 0735, as estimated from the shock model, is 1.7×10^{46} ergs s^{-1} (McNamara et al. 2005), and the observed steep central metallicity profile is consistent with the findings of Heath et al. (2006) for jet simulations of comparable power. However, the cavities in MS 0735 would increase the jet power significantly, in which case the dredge up by the rising bubbles is expected to have a significant effect in flattening the metallicity gradient. If such outbursts are rare and we assume no continuous central metal injection, the fact that we observe a normal gradient could thus be interpreted as a lack of strong evidence for significant metal uplifting or mixing by the cavities in MS 0735. If instead, as discussed above, all clusters go through a similar phase, the observed agreement would not be surprising as the large outbursts would contribute to create the global cluster properties. Note, however,

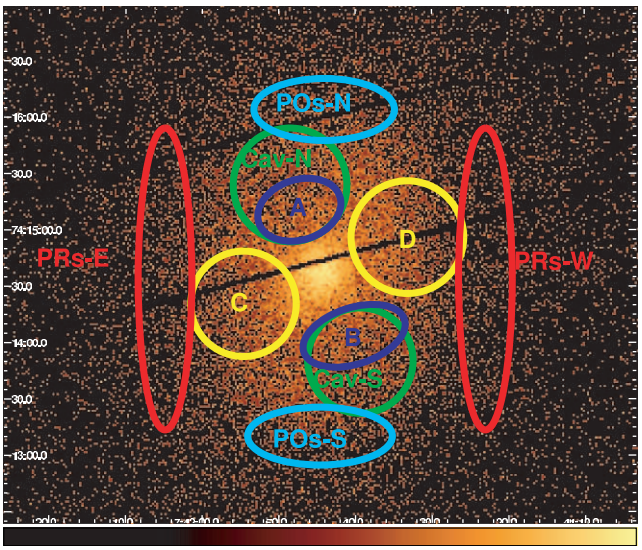

FIG. 26.—Regions considered to study the abundance distribution (see also the regions in Figs. 12 and 13).

that the existing models do not allow us to exclude the possibility of some dredging occurring in MS 0735. Indeed, the predictions of numerical simulations depend strongly on the details of the jet (like opening angle, initial Mach number, duration), which can significantly affect the extent of mixing. A direct comparison with the metallicity profile observed in MS 0735 would therefore require a tailoring of such simulations to the particular conditions of the outburst in this cluster. Furthermore, observations of broader metallicity profiles compared to the cD light profiles in cD clusters (De Grandi & Molendi 2001; David et al. 2001; Rebusco et al. 2005) indicate that some outward diffusion of enriched gas due to AGNs or mergers is occurring. Powerful outbursts such as the one in MS 0735 are more likely to produce such an effect. What we conclude from our analysis is therefore that the single outburst in MS 0735 has not appreciably affected the metal profile compared to other objects, although we cannot exclude the possibility of some mixing.

On the other hand, we note that when dealing with azimuthally averaged profiles we cannot study the local distribution of metals. In order to further investigate the metallicity distribution we extract the spectra in the regions indicated in Figure 26 and measure the abundance by fitting them with a `mekal` model. The results are reported in Table 8 and shown in Figure 27, where we also plot for comparison the azimuthally averaged profile. Simulations involving uplift by the cavities show that material is entrained at the upper (or lower) surface of the rising bubble and in its wake (e.g., Churazov et al. 2001), and the resulting metal distribution is very elongated along the direction of the bubbles (Roediger et al. 2007). We note that the possibility of making an accurate comparison between the pattern of abundance that we observe and the prediction of these models is complicated by the poor photon statistics, which do not allow us to place definite constraints on the metal distribution. Detailed abundance maps of the central cluster regions are required for this purpose.

7.4. *r-T Relation*

A tight size-temperature relationship is expected, as both of these quantities reflect the depth of the gravitational potential well in a virialized halo. Self-similarity predicts that $r_\Delta \propto (\langle T_X \rangle)^{1/2}$ (Mohr & Evrard 1997). Studies of ensembles of simulated clusters have confirmed this proportionality, providing a value for the normalization in the relation (e.g., Evrard et al. 1996). Recent *XMM-Newton* observations of a sample of six relaxed galaxy clusters hotter than 3.5 keV find for an overdensity $\Delta = 2500$ that (Arnaud et al. 2005):

$$h(z) r_{2500} = (500 \pm 5)\ \mathrm{kpc} \left(\frac{\langle T_X \rangle}{5\ \mathrm{keV}} \right)^{0.50 \pm 0.03} \quad (9)$$

TABLE 8
MEASURED ABUNDANCES

Region	Z ($Z_\odot$)	χ^2/dof
PRs-E	$0.34^{+0.33}_{-0.29}$	143/122
PRs-W	$0.44^{+0.36}_{-0.30}$	87/100
POs-N	$0.27^{+0.26}_{-0.22}$	116/110
POs-S	$0.25^{+0.26}_{-0.24}$	113/118
Cav-N	$0.31^{+0.12}_{-0.11}$	394/313
Cav-S	$0.28^{+0.12}_{-0.11}$	288/287
A	$0.54^{+0.22}_{-0.20}$	188/174
B	$0.30^{+0.16}_{-0.15}$	173/210
C	$0.36^{+0.09}_{-0.10}$	346/380
D	$0.37^{+0.11}_{-0.11}$	371/335
(PRs-E) + (PRs-W)	$0.42^{+0.23}_{-0.20}$	301/227
(POs-N) + (POs-S)	$0.25^{+0.17}_{-0.16}$	233/233
(Cav-N) + (Cav-S)	$0.30^{+0.08}_{-0.08}$	869/605
A + B	$0.40^{+0.13}_{-0.12}$	497/389
C + D	$0.36^{+0.07}_{-0.07}$	902/720

NOTES.—Abundance measured in the regions indicated in Fig. 26. The `mekal` fit is performed in the [0.4–10.0] keV energy range by fixing the absorbing column density to the Galactic value. When fitting simultaneously two different regions at the same radial distance from the center (e.g., C+D), the normalizations of each camera are linked in order to have the same value in the two regions. Error bars are at the 90% confidence levels on a single parameter of interest.

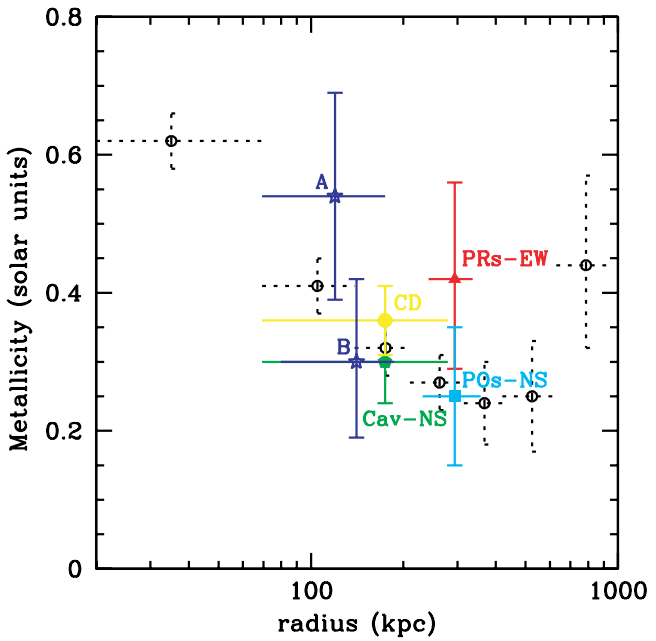

FIG. 27.—Abundances measured in different regions are indicated with the same color scheme used to define the regions in Fig. 26. For comparison, the azimuthally averaged metallicity profile is also shown (*open circles*). The error bars are at the 1 σ level.

where the factor $h(z)$ corrects for the evolution expected in the standard self-similar model (see eq. [7]). In the case of MS 0735 the scaling factor is small, being $h(z) = 1.11$ at $z = 0.216$. This relation allows us to estimate a value of $r_{2500} \sim 440 \pm 5$ kpc, which is consistent with the value of $r_{2500} = 463 \pm 65$ kpc determined from the overdensity profile (see § 7.1). We therefore find no evidence that the outburst is visibly affecting the size-temperature relationship.

We note that different studies on samples of galaxy clusters find that the r_Δ-T relation, as deduced from simulated clusters (Evrard et al. 1996), deviates systematically from the measured values of r_Δ, as inferred from the overdensity profile (Sanderson et al. 2003; Piffaretti et al. 2005). The largest discrepancy is found for $\Delta = 200$ and in the smallest halos. Our result, derived for $\Delta = 2500$ in a massive cluster, does not contradict these findings. The estimate of r_{2500} is more reliable than that of r_{200} as it does not require much extrapolation of the universal NFW profile (see § 7.1). Furthermore, the impact of additional, nongravitational heating is minimal in massive clusters. Its effect is most pronounced in poor, cool clusters, where the extra energy required to account for their observed properties is comparable to their thermal energy (e.g., Ponman et al. 1996; Tozzi & Norman 2001).

7.5. *M-T Relation*

Theoretical predictions based on the simplistic assumption of an isothermal sphere for both the gas represented by its temperature and the collisionless dark matter particles (e.g., Kaiser 1986; Bryan & Norman 1998) infer a self-similar scaling relation between $M_{\rm tot}$ and T at a given overdensity in the form $M \propto T^{3/2}$. Various observational studies have found different and sometime conflicting results regarding the slope and normalization of the M-T relation (e.g., Allen et al. 2001; Finoguenov et al. 2001; Ettori et al. 2002; Sanderson et al. 2003, Arnaud et al. 2005, and references therein). The relation derived by Arnaud et al. (2005) for a subsample of six relaxed clusters hotter than 3.5 keV observed with *XMM-Newton* is consistent with the standard self-similar expectation, following the relation:

$$h(z)M_{2500} = (1.79 \pm 0.06) \times 10^{14}\ M_\odot \left(\frac{\langle T_{\rm X}\rangle}{5\ {\rm keV}}\right)^{1.51\pm0.11} \qquad (10)$$

This result is in agreement with *Chandra* observations (Allen et al. 2001). In the case of MS 0735, equation (10) turns into an estimate of $M_{2500} = (1.51 \pm 0.05) \times 10^{14}\ M_\odot$. By considering the whole *XMM-Newton* sample (10 clusters in the temperature range [2–9] keV), the relation steepens with a slope $\sim$1.70 (Arnaud et al. 2005), indicating a breaking of self-similarity. In this case, we estimate $M_{2500} = (1.41 \pm 0.05) \times 10^{14}\ M_\odot$. Although in better agreement with the M-T relation predicted from the cluster scaling laws, the mass estimate of $M_{2500} = (1.74 \pm 0.42) \times 10^{14}\ M_\odot$ as derived from the overdensity profile (see § 7.1) is still consistent with a steeper slope of the relation considering the large errors that we measure.

7.6. *L-T Relation and Preheating*

The observed relation between X-ray luminosity and gas temperature in clusters is steeper than expected if cluster growth were governed by gravity alone. This steepening is best explained by the addition of heat to the ICM, and it has been estimated that the excess energies required to reconcile models and observations lie in the range of 1–3 keV per particle (Wu et al. 2000). The additional non gravitational heating is thought to have been injected into the gas during an early epoch of star formation and AGN activity, and therefore it has been called "preheating." Despite this term, there are now strong indications that powerful AGN outbursts occurring at late times may contribute a significant fraction of the extra energy (McNamara et al. 2005; Nulsen et al. 2005a, 2005b). In particular, in the case of MS 0735 the driving energy of the shock as determined using a spherical hydrodynamic model is $E_s \approx 5.7 \times 10^{61}$ ergs (McNamara et al. 2005). The AGN outburst in this cluster is therefore heating the gas mass within 1 Mpc ($\sim 7.7 \times 10^{13}\ M_\odot$) at the level of about $\frac{1}{4}$ keV per particle. The heating level increases to $\sim$0.6 keV per particle when considering the gas mass within r_{2500}($M_{\rm gas,2500} \sim 2.9 \times 10^{13}\ M_\odot$). This is a substantial fraction of the 1–3 keV per particle of excess energy required to preheat the cluster.

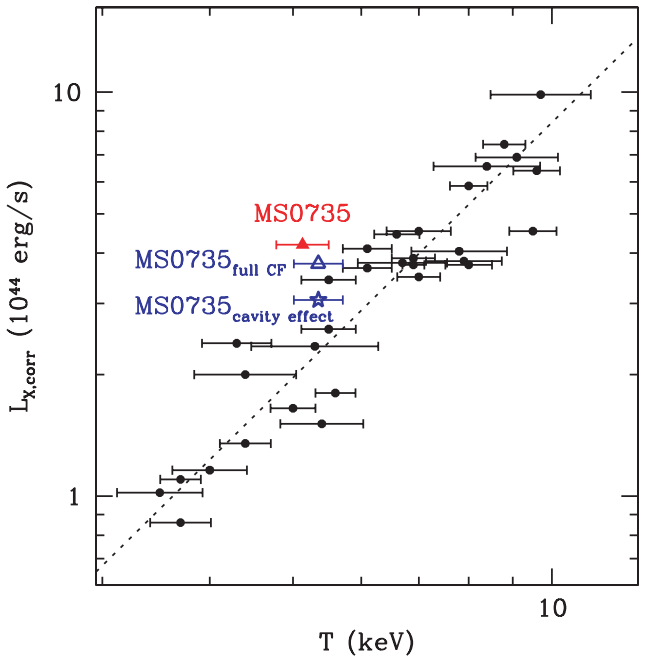

FIG. 28.—Luminosities in the 0.1–2.4 keV band corrected for the effect of cooling flow in the central $\sim$70 kpc vs. emission-weighted temperatures derived excluding cooling flow components, from Markevitch (1998). The red filled triangle represents MS 0735 data from the present observations corrected consistently with the method adopted by Markevitch (1998). The blue open triangle represents the MS 0735 data fully corrected for the effect of cooling flow (the cooling flow region in MS 0735 is bigger than the average value adopted by Markevitch [1998] for the cluster sample). We also show for interest the data corrected for the cavity effect (*blue open star*). See text for details.

In order to place MS 0735 in the observed luminosity versus temperature relation for galaxy clusters, we estimate that its X-ray luminosity in the 0.1–2.4 keV energy range is $L_{\rm X} \sim 5.0 \times 10^{44}$ ergs s^{-1}. For a total emission-weighted temperature of $kT = 4.4$ keV the observed luminosity is a factor $\sim$2.6 higher than that predicted by Markevitch's relation (Markevitch 1998). The departure of MS 0735 from the mean L-T relation is reduced when we correct both temperature and luminosity for the effect of the cooling flow, in the usual manner for the study of the scaling relations. In order to be fully consistent with the results presented by Markevitch (1998), we estimate the effect of the cooling flow by adopting the same approach of this author. The corrected temperature is obtained by averaging the projected temperature profile after excluding the coolest component in the central 20″ bin (as estimated from a multiphase spectral fit), resulting $kT \sim 5.1$ keV. The corrected luminosity is estimated from the flux observed by masking the central 20″ and then multiplying by a factor 1.06, which accounts for the flux of the hot plasma component inside the masked region. The corrected luminosity

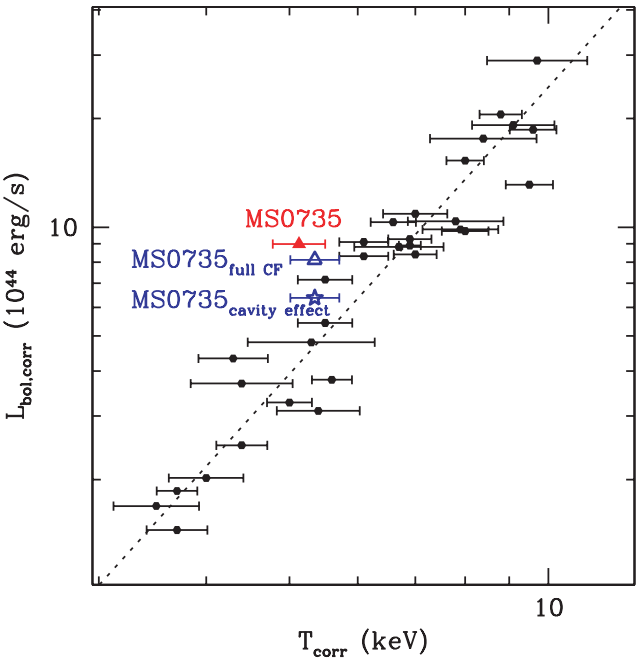

FIG. 29.—Same as Fig. 28, but for corrected bolometric luminosities.

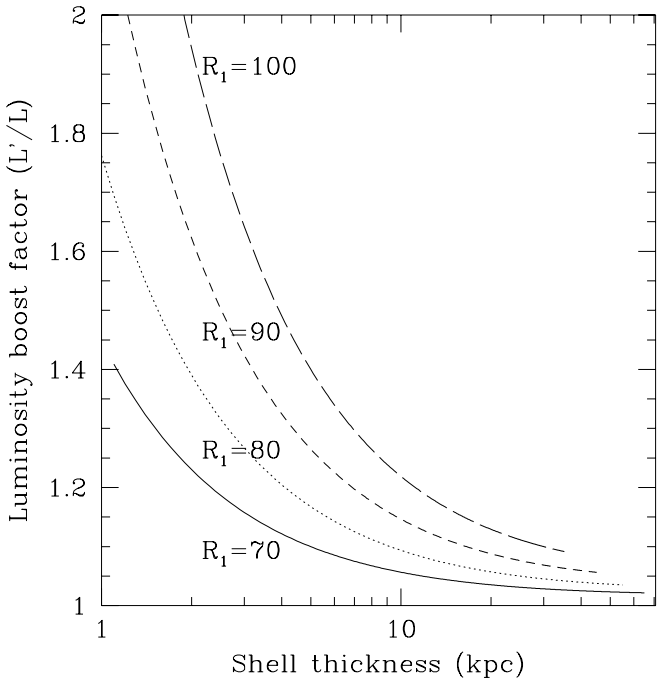

FIG. 30.—Estimated luminosity boost factor due to cavity expansion and gas compression in the shells, as a function of the thickness of the shell. Different curves refer to different radius R_1 of the cavities (units in kpc). In this simplified phenomenological model all the gas filling the cavities is assumed to be compressed into the bright shells. For an adiabatic index $\gamma = 5/3$, the maximum compression in a normal shock is a factor $f = 4$, so that the ratio of the shell thickness to the cavity radius is $R_2/R_1 - 1 > (1 + 1/f)^{1/3} - 1 \simeq 0.077$. For the cavities observed in MS 0735 ($R_1 \sim 100$ kpc), the shell thickness is $\sim$8 kpc, leading to a luminosity boost factor $\lesssim$25%.

in the 0.1–2.4 keV energy range is $L_X \sim 4.2 \times 10^{44}$ ergs s^{-1}, and the corrected bolometric luminosity is $L_{bol} \sim 9.0 \times 10^{44}$ ergs s^{-1}, which correspond to a factor $\sim$2 higher than expected from the corrected average temperature of the cluster.

Note that the cooling flow region in MS 0735 is bigger (see § 5.4) than the average value adopted by Markevitch (1998) for the cluster sample, and therefore the luminosities and temperature estimated above are not completely corrected for the effect of cooling flow. A more precise correction is obtained by estimating the luminosities from the spectra extracted after excluding the central 30″ and then adding back in the luminosity expected from a β-model profile inside the masked region. In this case we find values of $L_{[0.1-2.4]} \sim 3.8 \times 10^{44}$ ergs s^{-1} and $L_{bol} = 8.1 \times 10^{44}$ ergs s^{-1}. The temperature is estimated in a manner similar to the one described above, by averaging the temperature profile after excluding the coolest component in the central 30″ bin, resulting in $kT \sim 5.4$ keV. By considering these values "fully corrected" for the effect of cooling flow, the departure from the observed L-T relation is slightly reduced to a factor $\sim$1.7. The corrected luminosity versus temperature relations for luminosities estimated in the X-ray and bolometric bands are plotted in Figures 28 and 29, respectively. The MS 0735 representative points are shown as red filled triangles when corrected consistently with the method adopted by Markevitch (1998) and as blue open triangles when fully corrected for the effect of cooling flow. The results on temperatures and luminosities estimated in this section are summarized in Table 9.

TABLE 9

RESULTS FOR L-T RELATION

Band (keV)	Data	T (keV)	L_{obs} (10^{44} ergs s^{-1})	L^M_{rel} (10^{44} ergs s^{-1})
0.1–2.4.....	Total	4.4 ± 0.1	5.00	1.89
0.1–2.4.....	CF corr.^{M}	5.1 ± 0.4	4.19	2.07
0.1–2.4.....	CF fully corr.	5.4 ± 0.4	3.76	2.26
0.1–2.4.....	Cavity effect corr.	...	3.06	...
Bolometric.....	CF corr.^{M}	5.1 ± 0.4	8.98	4.20
Bolometric.....	CF fully corr.	5.4 ± 0.4	8.12	4.69
Bolometric.....	Cavity effect corr.	...	6.37	...

NOTES.—Temperatures and luminosities measured for MS 0735. The effect of the cooling flow (CF) has been evaluated by employing two different approaches. "CF corr.^{M}" indicates the correction adopted by Markevitch (1998): the temperature is obtained by averaging the temperature profile after excluding the coolest component in the central 20″ bin (as estimated from a multiphase spectral fit); the luminosities are estimated from the flux observed by masking the central 20″ and then multiplying by a factor 1.06 which accounts for the flux of the hot plasma component inside the masked region. "CF fully corr." indicates a more precise correction that takes into account the "true" extent of the cooling region in MS 0735: the temperature is estimated by averaging the temperature profile after excluding the coolest component in the central 30″ bin; the luminosities are estimated from the spectra extracted after excluding the central 30″ and then adding back in the luminosity expected from a β-model profile inside the masked region. L^M_{rel} indicates the luminosity expected from the luminosity vs. temperature relation (Markevitch 1998). The luminosities corrected for the cavity effect are also reported ("cavity effect corr."). See text (§ 7.6.1) for details.

7.6.1. *The "Cavity Effect"*

The energetic outburst and the consequently rising cavities uplift the central cool, low-entropy gas up to large radii, and at the same time the compression in the shells increases the ICM density. This effect of cooling flow, cavities, and bright shells (that for simplicity in the following we refer to as the "cavity effect") results in an increase of emissivity and thus luminosity. By considering a simple phenomenological model of the gas emissivity, which assumes that all the gas filling the cavities is compressed into the bright shells due to the cavity expansion, we estimate that the luminosity is boosted by a factor that depends on the cavity radius and shell thickness. For the particular configuration of the cavities observed in MS 0735, we expect an increase in luminosity by a factor as high as about 25% (see Fig. 30), consistent with our measurements. Note that since the cavities lie outside the cooling

region, their effect is not taken into account by the methods adopted above to correct for the cooling flow. The emission from the cavity region should also be masked before the average properties of the "undisturbed" cluster are estimated. We thus extract the spectra in the annular region $1.3'$–$6'$ (i.e., we excise the central $1.3'$ region, which includes the cavities). From these spectra we estimate $L_{[0.1-2.4]} \sim 3.1 \times 10^{44}$ and $L_{\rm bol} = 6.4 \times 10^{44}$ ergs s^{-1}, where the missing luminosity expected from a β-model profile inside the central masked region is added back in. A comparison of these values with those obtained by fully correcting for the effect of cooling flow allows us to evaluate the impact of the cavity effect on the luminosity (see Figs. 28 and 29, *blue open triangles and stars*). The observed luminosity increase is consistent with that expected by our simplified model of the structure and emissivity of the gas.

We want to stress that the cavity effect may contribute to partially explain the upward departure of MS 0735 from the mean L-T relation, accounting for $\lesssim$25% of the increased luminosity. It may also be relevant for the measurements of the gas mass fraction in galaxy clusters: the cavities create lumps in the ICM and this results in an increase of emissivity and therefore in an overestimate of the gas density. We find indeed some evidence that the gas mass fraction in MS 0735 might be higher than typically observed (see § 7.1).

8. CONCLUSIONS

The main conclusions of this work can be summarized as follows:

1. The energetic outburst in MS 0735 can heat the ICM up to a level of about $\frac{1}{4}$–$\frac{1}{2}$ keV per particle, depending on its radius of influence, thus contributing a substantial fraction of the 1–3 keV per particle of excess energy required to preheat the cluster (§ 7.6). Only a few outbursts of this magnitude erupting over the life of a cluster would be required to preheat it.

2. MS 0735 is a factor $\sim$2 more luminous than expected from its average temperature on the basis of the observed L-T relation for galaxy clusters (§ 7.6). Flux-limited samples of distant X-ray clusters may be biased in favor of detecting clusters with energetic outbursts.

3. The ICM compression in the bright shells due to the cavity expansion produces a boost of the central luminosity of a factor that we estimate should be $\lesssim$25%, consistent with our measurements (§ 7.6). This "cavity effect" may contribute to partially explain the upward departure of MS 0735 from the mean L-T relation and may also lead to an overestimate of the gas mass fraction in qualitative agreement with the high value of $f_{\rm gas,2500}$ that we measure for MS 0735 (§ 7.1).

4. The observed scaled temperature and metallicity profiles are in general agreement with those observed in relaxed clusters (§§ 7.2 and 7.3). Also, the quantities we measure for MS 0735 are consistent with the r-T and M-T relations predicted by the cluster scaling laws (§§ 7.4 and 7.5). This probably indicates that violent outbursts such as the one in MS 0735 do not cause gross instantaneous departures from the average cluster profiles and cluster scaling relations (other than the L-T relation). However, if they are relatively common they may play a role in shaping these global properties.

It is nevertheless hard to draw general conclusions from only one object, and therefore in the future we plan to observe and study more supercavity systems.

We thank the anonymous referee for helpful comments that improved the paper. We thank S. Ettori for providing the software required to produce the X-ray color map in Figure 4. We thank S. Allen, A. Vikhlinin, and S. De Grandi for sending the data used to make the plots in Figures 23, 24, and 25. M. G. thanks F. Brighenti and B. Maughan for useful comments on the original manuscript. This research is supported by grant NNG056K87G from NASA's Goddard Space Flight Center and by NASA Long Term Space Astrophysics Grant NAG4-11025.

REFERENCES

Allen, S. W., Schmidt, R. W., & Fabian, A. C. 2001, MNRAS, 328, L37
———. 2002, MNRAS, 334, L11
Anders, E., & Grevesse, N. 1989, Geochim. Cosmochim. Acta, 53, 197
Arnaud, M., & Evrard, A. E. 1999, MNRAS, 305, 631
Arnaud, M., Neumann, D. M., Aghanim, N., Gastaud, R., Majerowicz, S., & Hughes, J. P. 2001, A&A, 365, L80
Arnaud, M., Pointecouteau, E., & Pratt, G. W. 2005, A&A, 441, 893
Arnaud, M., et al. 2002, A&A, 390, 27
Benson, A. J., Bower, R. G., Frenk, C. S., Lacey, C. G., Baugh, C. M., & Cole, S. 2003, ApJ, 599, 38
Bîrzan, L., Rafferty, D. A., McNamara, B. R., Wise, M. W., & Nulsen, P. E. J. 2004, ApJ, 607, 800
Blanton, E. L., Sarazin, C. L., & McNamara, B. R. 2003, ApJ, 585, 227
Blanton, E. L., Sarazin, C. L., McNamara, B. R., & Wise, M. W. 2001, ApJ, 558, L15
Böhringer, H., Voges, W., Fabian, A. C., Edge, A. C., & Neumann, D. M. 1993, MNRAS, 264, L25
Borgani, S., Governato, F., Wadsley, J., Menci, N., Tozzi, P., Quinn, T., Stadel, J., & Lake, G. 2002, MNRAS, 336, 409
Brighenti, F., & Mathews, W. G. 2003, ApJ, 587, 580
Brüggen, M. 2002, ApJ, 571, L13
Brüggen, M., & Kaiser, C. R. 2001, MNRAS, 325, 676
Bryan, G. L., & Norman, M. L. 1998, ApJ, 495, 80
Cavaliere, A., & Fusco-Femiano, R. 1976, A&A, 49, 137
Churazov, E., Forman, W., Jones, C., & Böhringer, H. 2000, A&A, 356, 788
Churazov, E., Brüggen, M., Kaiser, C. R., Böhringer, H., & Forman, W. 2001, ApJ, 554, 261
Clarke, T. E., Sarazin, C. L., Blanton, E. L., Neumann, D. M., & Kassim, N. E. 2005, ApJ, 625, 748
David, L. P., et al. 2001, ApJ, 557, 546
De Grandi, S., & Molendi, S. 2001, ApJ, 551, 153
De Young, D. 2006, ApJ, 648, 200
Dickey, J. M., & Lockman, F. J. 1990, ARA&A, 28, 215
Domainko, W., Gitti, M., Schindler, S., & Kapferer, W. 2004, A&A, 425, L21
Donahue, M., & Stocke, J. T. 1995, ApJ, 449, 554
Donahue, M., Stocke, J. T., & Gioia, I. M. 1992, ApJ, 385, 49
Dunn, R. J. H., Fabian, A. C., & Taylor, G. B. 2005, MNRAS, 364, 1343
Eke, V. R., Cole, S., & Frenk, C. S. 1996, MNRAS, 282, 263
Eke, V. R., Navarro, J. F., & Frenk, C. S. 1998, ApJ, 503, 569
Ettori, S., De Grandi, S., & Molendi, S. 2002, A&A, 391, 841
Evrard, A. E., & Henry, J. P. 1991, ApJ, 383, 95
Evrard, A. E., Metzler, C. A., & Navarro, J. F. 1996, ApJ, 469, 494
Fabian, A. C. 2003, MNRAS, 344, L27
Fabian, A. C., Voigt, L. M., & Morris, R. G. 2002, MNRAS, 335, L71
Fabian, A. C., et al. 2000, MNRAS, 318, L65
Finoguenov, A., Reiprich, T. H., & Böhringer, H. 2001, A&A, 368, 749
Ghizzardi, S. 2001, In Flight Calibration of the PSF for the MOS1 and MOS2 Cameras (XMM-SOC-CAL-TN-0022; Madrid: ESA), http://xmm.vilspa.esa.es/external/xmm_sw_cal/calib/documentation/index.shtml
Gitti, M., Feretti, L., & Schindler, S. 2006, A&A, 448, 853
Heath, D., Krause, M., Alexander, P. 2007, MNRAS, 374, 787
Heinz, S., Choi, Y.-Y., Reynolds, C. S., & Begelman, M. C. 2002, ApJ, 569, L79
Johnstone, R. M., Allen, S. W., Fabian, A. C., & Sanders, J. S. 2002, MNRAS, 336, 299
Kaiser, C. R., & Binney, J. 2003, MNRAS, 338, 837
Kaiser, N. 1986, MNRAS, 222, 323
Lacey, C., & Cole, S. 1993, MNRAS, 262, 627
Lin, Y.-T., Mohr, J. J., & Stanford, S. A. 2003, ApJ, 591, 749
Lumb, D. H., Warwick, R. S., Page, M., & De Luca, A. 2002, A&A, 389, 93
Markevitch, M. 1998, ApJ, 504, 27

Markevitch, M., Vikhlinin, A., & Mazzotta, P. 2001, ApJ, 562, L153
Mazzotta, P., Kaastra, J. S., Paerels, F. B., Ferrigno, C., Colafrancesco, S., Mewe, R., & Forman, W. R. 2002, ApJ, 567, L37
McNamara, B. R., Nulsen, P. E. J., Wise, M. W., Rafferty, D. A., Carilli, C., Sarazin, C. L., & Blanton, E. L. 2005, Nature, 433, 45
McNamara, B. R., et al. 2000, ApJ, 534, L135
———. 2001, ApJ, 562, L149
Mohr, J. J., & Evrard, A. E. 1997, ApJ, 491, 38
Navarro, J. F., Frenk, C. S., & White, S. D. M. 1996, ApJ, 462, 563
Nulsen, P. E. J., Hambrick, D. C., McNamara, B. R., Rafferty, D., Bîrzan, L., Wise, M. W., & David, L. P. 2005a, ApJ, 625, L9
Nulsen, P. E. J., McNamara, B. R., Wise, M. W., & David, L. P. 2005b, ApJ, 628, 629
Omma, H., Binney, J., Bryan, G., & Slyz, A. 2004, MNRAS, 348, 1105
Peterson, J. R., et al. 2003, ApJ, 590, 207
Pfrommer, C., Enßlin, T. A., & Sarazin, C. L. 2005, A&A, 430, 799
Piffaretti, R., Jetzer, P., Kaastra, J. S., & Tamura, T. 2005, A&A, 433, 101
Pollack, L. K., Taylor, G. B., & Allen, S. W. 2005, MNRAS, 359, 1229
Ponman, T. J., Bourner, P. D. J., Ebeling, H., & Böhringer, H. 1996, MNRAS, 283, 690
Rafferty, D., McNamara, B. R., Nulsen, P. E. J., & Wise, M. W. 2006, ApJ, 652, 216
Readhead, A. C. S., et al. 2004, Science, 306, 836
Rebusco, P., Churazov, E., Böhringer, H., & Forman, W. 2005, MNRAS, 359, 1041
Roediger, E., Brueggen, M., Rebusco, P., Boehringer, H., & Churazov, E. 2007, MNRAS, 375, 15
Rosner, R., & Tucker, W. H. 1989, ApJ, 338, 761
Ruszkowski, M., & Begelman, M. C. 2002, ApJ, 581, 223
Sanderson, A. J. R., Ponman, T. J., Finoguenov, A., Lloyd-Davies, E. J., & Markevitch, M. 2003, MNRAS, 340, 989
Schindler, S., Castillo-Morales, A., De Filippis, E., Schwope, A., & Wambsganss, J. 2001, A&A, 376, L27
Spergel, D. N., et al. 2003, ApJS, 148, 175
Tabor, G., & Binney, J. 1993, MNRAS, 263, 323
Tozzi, P., & Norman, C. 2001, ApJ, 546, 63
Tucker, W. H., & Rosner, R. 1983, ApJ, 267, 547
Vikhlinin, A., Kravtsov, A., Forman, W., Jones, C., Markevitch, M., Murray, S. S., & Van Speybroeck, L. 2006, ApJ, 640, 691
Vikhlinin, A., Markevitch, M., Murray, S. S., Jones, C., Forman, W., & Van Speybroeck, L. 2005, ApJ, 628, 655
Voigt, L. M., & Fabian, A. C. 2006, MNRAS, 368, 518
Voigt, L. M., Schmidt, R. W., Fabian, A. C., Allen, S. W., & Johnstone, R. M. 2002, MNRAS, 335, L7
Voit, G. M. 2005, Rev. Mod. Phys., 77, 207
Voit, G. M., & Donahue, M. 2005, ApJ, 634, 955
White, S. D. M., & Rees, M. J. 1978, MNRAS, 183, 341
Wise, M. W., et al. 2007, ApJ, 659, 1153
Wu, K. K. S., Fabian, A. C., & Nulsen, P. E. J. 2000, MNRAS, 318, 889
Zakamska, N. L., & Narayan, R. 2003, ApJ, 582, 162